

Design and analysis of a Polar-Orbiting Gravimetry CubeSat-1

A Major Qualifying Project Report

Submitted to the faculty of
WORCESTER POLYTECHNIC INSTITUTE
In Partial Fulfillment of the Requirements for the
Degree of Bachelor of Science
in Aerospace Engineering
by



Jackson Neu



Ellie Sherman

Approved by:



Zachary R. Taillefer, Advisor

Assistant Professor of Teaching, Aerospace Engineering Department

“This report represents the work of one or more WPI undergraduate students submitted to the faculty as evidence of completion of a degree requirement. WPI routinely publishes these reports on its web site without editorial or peer review.”

Abstract

This project reports on the conceptual design of a 12U CubeSat mission for mapping the earth's gravity field, referred to as the Polar Orbiter Gravimetry Satellite (POGSat). The mission uses a pair of identical satellites carrying a gradiometer payload. The pair of satellites will orbit at two inclinations of 91° and 103° at an altitude of 260 km. The mission will generate a complete map of the gravity field every month, with a spatial half-wavelength resolution of 100 km, matching the spatial resolution established by the Gravity Field and Steady State Ocean Circulation Explorer (GOCE). Orbital design and analysis were conducted using Systems Tool Kit (STK). A propulsion system was designed along with orbital maneuvers, and required propellant was calculated. It was determined a hall thruster using iodine propellant would provide ample performance for maintaining orbit parameters. Structural design and analysis were performed with SolidWorks and Ansys. The satellite conformed to the requirements of the dispenser system. Thermal analysis was conducted using STK and COMSOL Multiphysics. The internal thermal environment was verified to be safe for electronic operation. Radiation and space environment effects were analyzed with STK, and adequate radiation shielding was developed. This project also includes continuing the development of a Helmholtz cage for simulating the magnetic field a spacecraft would experience in orbit.

Table of Contents

Abstract	2
Table of Figures	6
Table of Tables	8
Table of Authorship	9
1. Introduction.....	10
1.1. Mission Objective.....	10
1.2. Project Management.....	10
1.3. Background.....	11
1.3.1. Gravimetry	11
1.3.2. Polar Gaps	12
1.3.3. GRACE and GRACE-FO.....	13
1.3.4. GOCE Mission	14
1.3.5. MAGIC	15
1.3.6. Principles of Gradiometer operation	16
1.4. Mission Design.....	20
1.4.1. Requirements.....	20
1.5. Optimal Orbit.....	22
1.6. Mission Architecture	22
1.7. Payload	25
1.7.1. Accelerometer Instrument	27

2.	Mechanical Design and Analysis.....	30
2.1.	Deployment Mechanism Selection.....	30
2.2.	Mechanical Requirements.....	31
2.3.	Structural Frame.....	34
2.4.	Solar Arrays.....	35
2.5.	Subsystem Components.....	38
2.6.	Vibration Analysis.....	40
3.	Propulsion.....	46
3.1.	Types of Propulsion.....	46
3.2.	Thruster Trade Study.....	46
3.2.1.	Dual-Mode Configuration.....	47
3.2.2.	Single-Mode Propulsion System.....	48
3.3.	Preliminary Phase One Orbital Analysis.....	50
3.4.	Propulsion System Selection and Design.....	52
3.4.1.	Propellant Feed System Design.....	53
3.5.	Orbital Analysis.....	55
3.5.1.	Preliminary Lifetime Analysis without Station-keeping.....	55
3.5.2.	Preliminary Lifetime Analysis with Station-keeping.....	58
3.5.3.	Recommendations and Mission Considerations.....	60
4.	Environmental Analysis.....	61
4.1.	Analysis of Radiation Effects and Design Considerations.....	61

4.2.	Analysis of Micrometeorite Effects and Design Considerations.....	64
5.	Thermal Analysis.....	67
5.1.	SEET Thermal Analysis.....	68
5.2.	COMSOL Simulation.....	69
6.	Societal and Environmental Impacts.....	72
7.	Helmholtz Cage.....	73
8.	Conclusions.....	75
9.	References & Bibliography.....	76
10.	Appendices.....	85
	Appendix A.....	85
	Appendix B.....	86
	Appendix C.....	87

Table of Figures

Figure 1.1 Gradiometer Payload with Labeled Axes	26
Figure 1.2 Center of mass for fully fueled (left) and dry (right) POGSat.....	27
Figure 1.3: Close-Up View of Quartz Wafer [24]	27
Figure 1.4: Implementation of Quartz Wafer in Sensor [24].....	28
Figure 2.1: The CSD in 3U, 6U, and 12U forms [25].....	31
Figure 2.2 Maximum Payload Dimensions [26].....	32
Figure 2.3 View of tab gap in frame side panel.....	33
Figure 2.4: POGSat external structure	35
Figure 2.5: Solar array mid-deployment	36
Figure 2.6 Solar arrays at varying angles.....	37
Figure 2.7: Deployed solar arrays.....	37
Figure 2.8: Labeled view of internal components.....	39
Figure 2.9 Exploded view of components	39
Figure 2.10 Setup of Simulation in Ansys Workbench.....	41
Figure 2.11: Mesh of simulation model.....	42
Figure 2.12 Satellite Vibration Modes.....	43
Figure 2.13 First Satellite Mode Shape.....	43
Figure 2.14 Electron PSD Curve [21].....	44
Figure 2.15 Z-Axis Deformation	45
Figure 3.1: POGSat Propellant Feed Scheme	54
Figure 3.2: Finite Altitude Lowering Maneuver MCS.....	55
Figure 3.3: Automatic Sequence Required for Full-Sunlight Burn Constraint.....	56
Figure 3.4: STK Lifetime Analysis Tool estimate for altitude decay at 91° inclination.....	57
Figure 3.5: STK Lifetime Analysis Tool estimate for altitude decay at 103° inclination.....	57

Figure 3.6: STK Lifetime Analysis Tool estimate for Deorbiting at 91° inclination.....	57
Figure 4.1: STK SEET simulation of total accumulated radiation (rad) using aluminized mylar thicknesses of 0.25, 0.5, 0.75, and 1 mm	63
Figure 4.2: STK SEET Simulation of SEP Impact at Varying Energy Levels at 91° inclination.....	64
Figure 4.3: STK SEET Simulation of SEP Impact at Varying Energy Levels at 103° inclination.....	64
Figure 4.4: Impact Flux and Damaging Impact Flux vs Time at 91° Inclination	65
Figure 4.5: Impact Flux and Damaging Impact Flux vs Time at 103° Inclination	66
Figure 5.1 SEET Bulk Temperature with Aluminum Surface.....	68
Figure 5.2 SEET Bulk Temperature with Silver Beryllium Coating	69
Figure 5.3 Meshed Geometry of COMSOL Simulation	70
Figure 5.4 COMSOL Max and Min Temperatures.....	71
Figure 7.1: IDR-321 Geomagnetometer with Hall Probe, pictured with accessory Zero Gauss Chamber.	74

Table of Tables

Table 1.1: Mission Phase Diagram	25
Table 2.1: Dispenser Mechanism Selection	30
Table 2.2 Center of Mass Requirements [26]	32
Table 3.1: BGT-X5 Specifications [32]	47
Table 3.2: SiEPS Thruster Characteristics [33]	48
Table 3.3: NanoFEEP Thruster Characteristics [34]	48
Table 3.4: BHT-100 Thruster and LaB6 Cathode Characteristics [35],[36]	49
Table 3.5: NPT30-12-1U Thruster Characteristics [37]	49
Table 3.6: Thruster Trade Study Results	52
Table 3.7: POGSat Propellant Feed Scheme Component List	54
Table 3.8: Propulsion System maneuver timeline without station-keeping	58
Table 3.9: Propulsion System maneuver timeline with station-keeping	59
Table 4.1: Acceptable Radiation Dosage (krad) for Internal Hardware	62
Table 4.2: Maximum Impact and Mass Flux for Micrometeorite Particles over Mission Duration	66
Table 5.1 Component Operating Temperatures	67

Table of Authorship

Section	Main Author(s)	Secondary Author	Editor(s)
Introduction	All		Ellie Sherman
Background	All		Liam Piper
Mission Design	Ellie Sherman		Jackson Neu
Payload	Liam Piper	Ellie Sherman	Ellie Sherman
Mechanical Design and Analysis	Jackson Neu		Ellie Sherman
Propulsion	Ellie Sherman		Jackson Neu
Environmental Analysis	Ellie Sherman		Jackson Neu
Thermal Analysis	Jackson Neu		Ellie Sherman
Helmholtz Cage	Jackson Neu	Ellie Sherman	Ellie Sherman
Societal and Environmental Impacts	Ellie Sherman	Jackson Neu	Jackson Neu

1. Introduction

A CubeSat is a class of Satellite also known as MicroSats. CubeSats conform to a size formfactor made up of units which are 10x10x10cm cubes. Most commonly, CubeSats are categorized as 1U, 3U, 6U, or 12U in volume, although other configurations are possible. The CubeSat formfactor was developed by California Polytechnic State University to provide a platform for educational satellites [1]. The standardized small formfactor allows for relatively inexpensive satellite launches on rideshare missions.

1.1. Mission Objective

The primary objective of the POGSat mission is to map the Earth's gravitational field with complete global coverage over a period of approximately one month. The two satellites will be deployed to low earth orbits (LEO) of 260 km altitude, and inclinations of 91° and 103° . The two satellites at different inclinations will limit the data interpolation needed to account for coverage gaps, allowing for more accurate global coverage within a one-month period, with a reported 20% improvement in data reporting accuracy [2]. The continuously updated map of Earth's gravity measured by the satellites will allow the monitoring of mass movements on and within the earth, such as the melting of polar ice caps, or seismic activity [3]. Further detail regarding the societal impacts of the mission is provided in Section 6.

1.2. Project Management

For this project, spacecraft subsystems were assigned to the four students. Weekly meetings were held with the subsystem leads and with faculty advisors, acting as project managers to facilitate systems engineering between the teams. Spacecraft and mission requirements discussed in these meetings were implemented by the relevant subsystem leads. Outside of satellite design, the development of a Helmholtz Cage was assigned to Jackson Neu and Ellie Sherman. The development of a low friction test stand was split between Liam Piper and Ethan Prigge. Any purchases required are facilitated through Jackson Neu.

1.3. Background

Many aspects of this project are based on prior gravitational measuring satellite missions, such as GOCE and GRACE which are discussed below. Our mission aims to be the first Earth gravimetry satellite in the CubeSat formfactor. We seek to improve upon past missions by increasing mission duration and measurement accuracy.

1.3.1. Gravimetry

Gravimetry is the measurement of a gravitational field. For our mission, we will use a satellite to measure Earth's gravitational field strength and its variation with position and time. The gravitational acceleration due to Earth's gravity field has a relatively constant value of $9.81 \frac{m}{s^2}$, however there are slight variations in this acceleration due to the mass distribution of Earth. The most significant effect is caused by the oblate shape of the Earth; however, smaller gravitational anomalies exist due to varying density and topography. The strength of these anomalies is typically on the order of 300mGal, where $1 \text{ mGal} = 10^{-5} \frac{m}{s^2}$ [4].

Most models of the gravitational field use a spherical harmonic representation [5]. This model approximates the strength of the gravitational field with a sum of harmonics of varying strength and frequency, similar to a Fourier series. Computing the coefficients of each harmonic term provides an approximation of a gravity field that varies with latitude and longitude.

The study of Earth's gravity was a key area of science long before the first satellites were launched. Prior to the space age, gravimetric measurements were conducted with land-based equipment, however it was challenging to correlate measurements made by different instruments in various locations, and marine measurements were less accurate than those on land. Satellite based gravimetry allowed for complete global coverage with a single instrument [6].

1.3.2. Polar Gaps

Generally, high inclination orbits are used to provide global observational coverage, however these high inclination polar orbits can lead to less frequent coverage at lower latitudes. The GOCE mission opted for a 97° inclination orbit, which provides sufficient global coverage, but leaves a coverage gap at the Earth's poles [7]. In a single satellite configuration, this gap, as often termed “polar gaps” by researchers, is closed by an interpolation of the collected data, with the accuracy dependent on the amount of data collected and the size of the gap [2]. The gravity field from within these gaps can be recovered using a set spherical harmonic coefficient implemented into a spherical harmonic expansion, which allows for the calculation of a gravitational field given a set of position, velocity, and acceleration vectors. Equation 1.1 shows the spherical harmonic approximation of a gravity field [8].

$$V(\rho, \varphi, \lambda; \mathbf{u}) = \frac{GM}{\rho} \left[1 + \sum_{l=2}^{L_{MAX}} \sum_{m=0}^l \left(\frac{R_E}{\rho} \right)^l (\overline{C}_{lm} \cos(m\lambda) + \overline{S}_{lm} \sin(m\lambda)) * \overline{P}_{lm} \sin(\varphi) \right] \quad 1.1$$

Where V is the gravitational potential of a given point with radius ρ , latitude φ and longitude λ . G is the gravitational constant, M is the mass of the Earth, R_E is the Earth's radius, l and m are the degree and order of the spherical harmonic expansion. \overline{C}_{lm} and \overline{S}_{lm} are the spherical harmonic coefficients. \overline{P}_{lm} is the normalized associated Legendre function.

The recovered data calculated using the expansion formula is then compared to the collected gravitational field data to determine the accuracy of the full recovered gravity field.

Increasing the sample size reduces the amount of required data interpolation, which can be achieved by varying the inclination of orbits in a satellite constellation. A *bender double-pair* refers to a constellation of satellite pairs composed of one polar orbit with an additional pair, usually of a high inclination between 60° - 70° or 100° - 110°, added to collect more data and improve data resolution

within the middle latitude region, or -60° - 60° latitude [2]. While the polar orbiting satellite, in general, provides sufficient global coverage, the addition of the second pair improves coverage in middle latitudes while minimizing the polar gap, and decreases the time required to complete full global coverage. This formation is best utilized for missions that focus on geodesy, specifically within the polar region of 60° latitude and above.

1.3.3. GRACE and GRACE-FO

The Gravity Recovery And Climate Experiment (GRACE) mission was a joint mission between the National Aeronautics and Space Administration (NASA) and German Aerospace Center (DLR) with ground operations performed by the ESA and German Research Centre for Geosciences (GFZ) [10]. The GRACE satellite mission was created to monitor the Earth's gravitational field changes to map water and mass redistribution over time. The mission lasted from March 2002 to October 2017 [11]. After the GRACE mission concluded, a follow-up mission termed GRACE Follow-On (GRACE-FO) was launched in May 2018 with an identical mission description and similar payload with the goal of continuing GRACE's data collection efforts.

The primary instrumentation payload for GRACE included a three-axis capacitive accelerometer, which measures the non-gravitational forces acting on the pair of satellites as a function of their position [13]. Coupled with the accelerometer readings, a K-Band Ranging (KBR) System was installed to measure the distance between the leading and lagging satellites to measure the fluctuations in the gravitational field experienced by each satellite [11]. The true position of the satellites is confirmed using SST through the GPS constellation, which serves to establish the satellite's expected position at a given point within the satellites' orbit. The varying strength of the Earth's gravitational field will draw the leading satellite forward in its orbit, reflected by the by measurements from the onboard accelerometers and communicated between the satellites using the KBR System, allowing a map of the gravitational field to be constructed by mapping the orbital perturbations experienced by the GRACE satellite system.

The measurement accuracy obtained in the GRACE mission series was at a length of scale of 200 km at a $10^{-5} \frac{m}{s^2}$ scale [13].

1.3.4. GOCE Mission

The Gravity Field and Steady State Ocean Circulation Explorer (GOCE) was a satellite created by the European Space Agency (ESA) designed to monitor and map Earth's gravitational field. GOCE launched in March of 2009 into a low earth orbit of 260 km altitude. The mission ended in October 2013 [7].

The primary instrument of GOCE was the Electrostatic Gravity Gradiometer (EGG), which was used to create a map of earth's geoid. The EGG consisted of three pairs of highly sensitive accelerometers, mounted along three orthogonal axes, centered on the satellite's center of mass. The six accelerometers form an instrument known as a gradiometer. The axes of the gradiometer were aligned to be earth facing, along track (parallel to spacecraft velocity vector), and cross track (perpendicular to spacecraft velocity vector). By positioning the accelerometers away from the center of mass, it was possible to derive the variation in gravitational force along the arms of the gradiometer. These measurements are used to construct the gravity gradient tensor at the satellite's location. Equation 1.2 represents how the gravitational force vector changes along each spatial dimension. Using this gravity tensor, the shorter wavelength terms of the gravity field can be derived.

$$G = \nabla g = \begin{bmatrix} \frac{\partial g_x}{\partial x} & \frac{\partial g_x}{\partial y} & \frac{\partial g_x}{\partial z} \\ \frac{\partial g_y}{\partial x} & \frac{\partial g_y}{\partial y} & \frac{\partial g_y}{\partial z} \\ \frac{\partial g_z}{\partial x} & \frac{\partial g_z}{\partial y} & \frac{\partial g_z}{\partial z} \end{bmatrix} \quad 1.2$$

In addition to the gradiometer, GOCE employed Satellite to Satellite Tracking (SST) via GPS for additional gravity measurement. SST gravimetry works by precisely tracking the satellite's orbit using GPS, while measuring non-gravitational accelerations using onboard accelerometers. The GPS tracking of orbital perturbations can be used to derive differences in the gravitational force throughout the satellites orbit. [9]. The SST technique accurately measures the longer wavelength terms of the gravitational field. By combining the EGG and SST, GOCE measured Earth's gravity field with an accuracy of $10^{-5} \frac{m}{s^2}$ at a length scale of 100 km [14].

1.3.5. MAGIC

Conceptualized to improve the data collection efforts of GRACE, the Mass Change and Geoscience International Constellation (MAGIC) Satellite constellation is a dual satellite-pair configuration developed by the ESA for launch in 2028 [15]. Structurally similar to the GRACE and GRACE-FO missions, MAGIC will map the Earth's gravitational field by measuring the orbital perturbations communicated between each satellite pair. To improve collection accuracy, MAGIC seeks to implement the improved gradiometer payload introduced in the GOCE mission, using three accelerometers to calculate a gravitational gradient instead of the axis-specific gravitational readings from the GRACE mission series. The MAGIC mission is conceptualized to use a pseudo-bender constellation formation: composed of a pair of satellites that fly in an 89° polar orbit and a pair in a 70° high-inclined orbit. The validation for the addition of the second satellite pair is to improve coverage of the mid latitudes, decreasing the time required to achieve full global coverage [16]. Like previous gravitational mapping missions in the GRACE mission series, MAGIC will have an altitude of 340 km and 355 km, for the polar and inclined satellite pairs, respectively, to maximize the gravitational field strength experienced by the satellites.

1.3.6. Principles of Gradiometer operation

A gradiometer instrument consists of six accelerometers arranged in pairs along each axis of the gradiometer. We can label the six accelerometers as numbers 1-6, where the pair 1,4 is located along the x axis, the pair 2,5 is along the y axis, and 3,6 is along the z axis. Assuming an ideal gradiometer with no error in accelerometer positioning, the acceleration vectors measured by each accelerometer would be given by Equation 1.3 [17].

$$\mathbf{a}_i = -(\mathbf{G} - \mathbf{\Omega}^2 - \dot{\mathbf{\Omega}})\mathbf{r}_i + \mathbf{d} \quad 1.3$$

Where \mathbf{a}_i is the acceleration vector measured by the i-th accelerometer, \mathbf{G} is the gravity gradient matrix, $\mathbf{\Omega}$ is the angular velocity matrix of the spacecraft in the gradiometer frame, \mathbf{r}_i is the vector from the satellite center of mass (COM) to the i-th accelerometer, and \mathbf{d} is the linear acceleration of the satellite's COM. The measured acceleration is a combination of the linear acceleration of the COM and the acceleration due to the rotation of the spacecraft.

The accelerations are read as common mode (CM) or differential mode (DM) for each pair of opposite accelerometers. The CM and DM accelerations are given by Equation 1.4.

$$\mathbf{a}_{c,ij} = \frac{1}{2}(\mathbf{a}_i + \mathbf{a}_j) \quad 1.4$$

$$\mathbf{a}_{d,ij} = \frac{1}{2}(\mathbf{a}_i - \mathbf{a}_j)$$

Where $a_{c,ij}$ is the CM acceleration and $a_{d,ij}$ is the DM acceleration for each accelerometer pair ij . We can define the vector \mathbf{r}_i to be the difference of a vector \mathbf{p}_i from the origin of the gradiometer to the

i-th accelerometer, and the vector c from the COM to the origin of the gradiometer. Equation 1.5 demonstrates this relationship.

$$\mathbf{r}_i = \mathbf{p}_i - \mathbf{c} \quad 1.5$$

Combining Equations 1.3, 1.4, and 1.5 gives the relationship shown in Equation 1.6.

$$\mathbf{a}_{c,ij} = -\frac{1}{2}(\mathbf{G} - \mathbf{\Omega}^2 - \dot{\mathbf{\Omega}})(\mathbf{p}_i + \mathbf{p}_j) + (\mathbf{G} - \mathbf{\Omega}^2 - \dot{\mathbf{\Omega}})\mathbf{c} + \mathbf{d} \quad 1.6$$

$$\mathbf{a}_{d,ij} = -\frac{1}{2}(\mathbf{G} - \mathbf{\Omega}^2 - \dot{\mathbf{\Omega}})(\mathbf{p}_i - \mathbf{p}_j)$$

For each opposite pair of accelerometers, the relations in Equation 1.7 hold for an ideal gradiometer.

$$\mathbf{p}_i + \mathbf{p}_j = \begin{bmatrix} 0 \\ 0 \\ 0 \end{bmatrix} \quad 1.7$$

$$\mathbf{p}_1 - \mathbf{p}_{j4} = \begin{bmatrix} L_x \\ 0 \\ 0 \end{bmatrix}$$

$$\mathbf{p}_2 - \mathbf{p}_5 = \begin{bmatrix} 0 \\ L_y \\ 0 \end{bmatrix}$$

$$\mathbf{p}_3 - \mathbf{p}_6 = \begin{bmatrix} 0 \\ 0 \\ L_z \end{bmatrix}$$

Where L_x, L_y, L_z are the distances between the accelerometer pairs along the x, y, and z axes. By combining Equations 1.6 and 1.7, we can write the common mode acceleration as given by Equation 1.8.

$$a_{c,ij} = (\mathbf{G} - \Omega^2 - \dot{\Omega})\mathbf{c} + \mathbf{d} \quad 1.8$$

If the center of the gradiometer is positioned to be close to the COM, such that the distance $c \cong 0$ the common mode acceleration simplifies to Equation 1.9.

$$a_{c,ij} = \mathbf{d} \quad 1.9$$

We can also simplify the differential mode accelerations, as depicted by Equation 1.10.

$$A_d = \frac{-1}{2} (\mathbf{G} - \Omega^2 - \dot{\Omega}) \quad 1.10$$

Where $A_d = [a_{d,14}, a_{d,25}, a_{d,36}]$ and $L = \begin{bmatrix} L_x & 0 & 0 \\ 0 & L_y & 0 \\ 0 & 0 & L_z \end{bmatrix}$. It can be shown that V and Ω^2 are

symmetric matrices, and $\dot{\Omega}$ is skew-symmetric. Using these properties, Equation 1.11 proves that:

$$A_d L^{-1} - (A_d L^{-1})^T = \dot{\Omega} \quad 1.11$$

$$A_d L^{-1} + (A_d L^{-1})^T = -\mathbf{G} + \Omega^2$$

The components of the gravity gradient can then be obtained from the differential mode accelerations and the angular velocity as given by Equation 1.12 [17].

$$G_{xx} = -2 \frac{a_{d,14}}{L_x} - \omega_y^2 - \omega_z^2 \quad 1.12$$

$$G_{yy} = -2 \frac{a_{d,25}}{L_y} - \omega_x^2 - \omega_z^2$$

$$G_{zz} = -2 \frac{a_{d,36}}{L_z} - \omega_y^2 - \omega_x^2$$

$$G_{xy} = -\frac{a_{d,25}}{L_y} - \frac{a_{d,14}}{L_x} + \omega_x \omega_y$$

$$G_{xz} = -\frac{a_{d,36}}{L_z} - \frac{a_{d,14}}{L_x} + \omega_x \omega_z$$

$$G_{yz} = -\frac{a_{d,25}}{L_y} - \frac{a_{d,36}}{L_z} + \omega_z \omega_y$$

1.4. Mission Design

Each subsystem has outlined a set of requirements and constraints for the mission.

1.4.1. Requirements

Payload

- Payload should have measurement accuracy of $10^{-5} \frac{m}{s^2}$ at a half wavelength scale of 100 km
- Accelerometer axes must be aligned to be Earth facing, parallel to the velocity vector, and perpendicular to the velocity vector
- Gradiometer origin must be aligned to the center of mass

Mechanical

- Design a structure to house the payload, propulsion system, and electrical components
- Ensure spacecraft conforms to the launch vehicle and deployment system requirements
- The structure must conform to the 12U CubeSat formfactor and mechanical requirements of the Canisterized Satellite Dispenser
- The structure must satisfy the vibrational and loading requirements of the dispenser, not exceeding 3560N of force on both tabs.
- Spacecraft center of mass must be less than 40mm from geometric origin during launch

Power

- Must provide enough power to support subsystem needs throughout mission duration
- CubeSat will be powered from onboard solar cells
- The power team must provide power to all systems for the full duration of the mission

Propulsion

- The propulsion system must operate under the limitations established by the power and structures subsystems
- The propulsion system will provide the necessary thrust, ΔV , and specific impulse to fulfill the mission requirements
- The propulsion subsystem must compensate for orbital perturbations, primarily drag, during Phase 2 to extend mission duration
- The propulsion subsystem must deorbit within the 5-year period after the mission concludes

ADCS

- ADCS will have a pointing accuracy of 0.1 degrees
- The ADCS System will be able to detumble within 2 orbits of being activated
- Must have the capability to be able to run while the payload is activated, collecting scientific data

GNC

- Communications system will be able to downlink and uplink with a speed of at least $1 \frac{kb}{s}$
- GPS must have a 1-5cm location accuracy
- Overly capable for the needs of data transmission and remote updates
- Communications system will be doubly redundant

Space Environments

- CubeSat will be designed to operate for mission duration considering expected radiation at operational altitude
- CubeSat will be designed to operate for mission duration considering micro-meteoroid field conditions at operational altitude

- Outer shell must be thick enough to prevent internal radiation and impact damage to internal components

Thermal

- CubeSat will be designed to operate for mission duration in an ambient thermal environment
- CubeSat thermal design will accommodate for survivability and operating temperature range for all components
- Temperature sensitive components will be kept in a temperature-controlled area of the CubeSat

1.5. Optimal Orbit

The optimal orbit for a gravitational field mapping mission should maintain a low altitude or extreme low earth orbit (eLEO) and have high inclination for global coverage. The payload requires that one accelerometer pair be constantly Earth-facing to establish a functional gravity gradient. To maximize the experienced gravity on the satellite, the CubeSat will maintain a constant 260 km altitude. In addition to the primary 91° orbiting CubeSat, an additional CubeSat at a 103° inclination is needed to reduce the time required to establish global coverage from 32 days to 11 days. This modified Bender configuration will optimize the amount of gravitational field measured such that monthly field readings can be provided to researchers for a three-month sampling basis, which is typical for yearly ice-flow measurements [18].

1.6. Mission Architecture

The mission is split into phases based on different mission objectives throughout the duration of the mission. Due to the 12° inclination change required for a single deployment, to reduce the propellant mass required to complete the mission the CubeSats will be deployed on two different rideshare missions. As such, each deployment will be assumed to occur at or close to the two desired inclinations as specified in Section 1.5.

As part of the mission plan, an appropriate launch vehicle was required to bring POGSat into orbit. Many launch vehicles have the capability to deploy a lightweight CubeSat into low earth orbit, and most launch providers offer rideshare services for SmallSat missions. Ridesharing lowers the barrier to entry by reducing the cost of launch for secondary payloads, such as CubeSats. For this mission, only flight-proven vehicles such as the Falcon 9, Electron, and Atlas 5, all of which have flown with the necessary satellite dispenser. The Atlas 5 rocket is soon to be retired, so a selection was made between the Falcon and Electron. Both vehicles can support the mission as part of a rideshare launch and have excellent flight heritage. Ultimately, the Electron rocket was selected as the best fit for the mission. The Electron is specifically designed for SmallSat launches and rideshare missions, having completed 11 SmallSat rideshare missions [19]. The Canisterized Satellite Dispenser chosen for the deployment of POGSat is made by Planetary Systems Corporation, a subsidiary of Rocket Lab, meaning the dispenser is easily integrated onto the Electron rocket. Finally, the Electron has a unique third stage called the “Kick Stage”, which is designed to perform orbital adjustments for rideshare missions, so satellites can be deployed to multiple desired orbits in one mission [20]. This capability allows the POGSats to deploy close to the target orbits. When launching from Launch Complex 1 in New Zealand, Electron can target orbital inclinations from 39° to 120° , and altitudes from 400 km to 1100 km [21].

Upon deployment from the satellite dispenser, the CubeSats will begin Phase Zero, categorized by each CubeSat performing a detumbling maneuver and system health check. To perform a detumbling maneuver, the CubeSats will use onboard magnetorquers to counteract the angular velocity induced by ejection from the CSD. In addition to the detumbling maneuver, the onboard computer will perform a communication and systems check, ensuring that the ADCS system and payload accelerometers are within functional capacity. This detumbling phase is critical to ensuring control of the CubeSat, as reducing the angular velocity will permit further attitude control to take place.

After Phase Zero is completed, the CubeSats complete a series of transfer orbits and plane changes to establish their intended inclination and altitude. Phase One is composed of an orbit lowering

maneuver, wherein the CubeSats will maneuver into their target altitude and inclination, a polar orbit of 91° and high inclined orbit of 103° , both at a 260 km altitude. Provided an ideal deployment, the launch vehicle will deploy each POGSat at their desired inclination at an altitude of 500 km, where each POGSat will perform an orbit lowering maneuver. If any additional inclination changes are necessary, it would occur within Phase One.

Once the POGSats are in their optimal orbit, Phase Two will begin. This phase is where the satellite will carry out its primary mission of taking gravity measurements. Phase Two involves station-keeping and drag compensation maneuvers necessary to prolong the data collecting portion of the mission. Station-keeping maneuvers will consist of orbit raising to maintain the target 260 km. Due to the extreme Low Earth Orbit (eLEO) altitude achieved by the CubeSats within this mission, drag compensation will need to be performed to maintain the ideal orbit for data collection.

After Phase Two concludes, the CubeSats will need to deorbit within 5 years in accordance with FCC regulations [22]. Within Phase Three, CubeSats will perform a final orbit lowering maneuver to reduce altitude to 75 km, which is the accepted altitude that most satellites deteriorate upon reentry [23]. Table 1.1 summarizes the mission phases and maneuvers.

Table 1.1: Mission Phase Diagram

Mission Phase	Maneuvers	Description
Phase Zero	Launch Vehicle Separation	Detumble satellites
	System Performance Check	Initialize onboard systems to confirm functionality
Phase One	Orbit Lowering	Reduce altitude from deployment to target altitude
	Plane Change	Adjust inclination from deployment inclination, if necessary
Phase Two	Gravimetry Mission	Perform gravitational field measurements
	Orbital Maintenance	Station-keeping burns to raise altitude
	Drag compensation	Eliminate non-gravitational forces experienced by the satellites
Phase Three	Deorbit	Lower orbit to incite burnout

1.7. Payload

The scientific payload for the mission is a three-axis gradiometer, similar to the instrument used on GOCE. The gradiometer is comprised of three paired accelerometers, which allow a differential measurement of the gravity field by the process outlined in Section 1.3.6. The accelerometer pairs are separated along the velocity vector (Z), earth facing vector (-Y), and cross-track vector (X), and intersect the center of mass. The accelerometers are separated by distances of 14.0, 17.7, and 16.8 cm across the X, Y, and Z axes respectively, forming the arms of the gradiometer. Figure 1.1 shows the gradiometer payload with the positive X, Y, and Z axes indicated. The six accelerometers are shown in black.

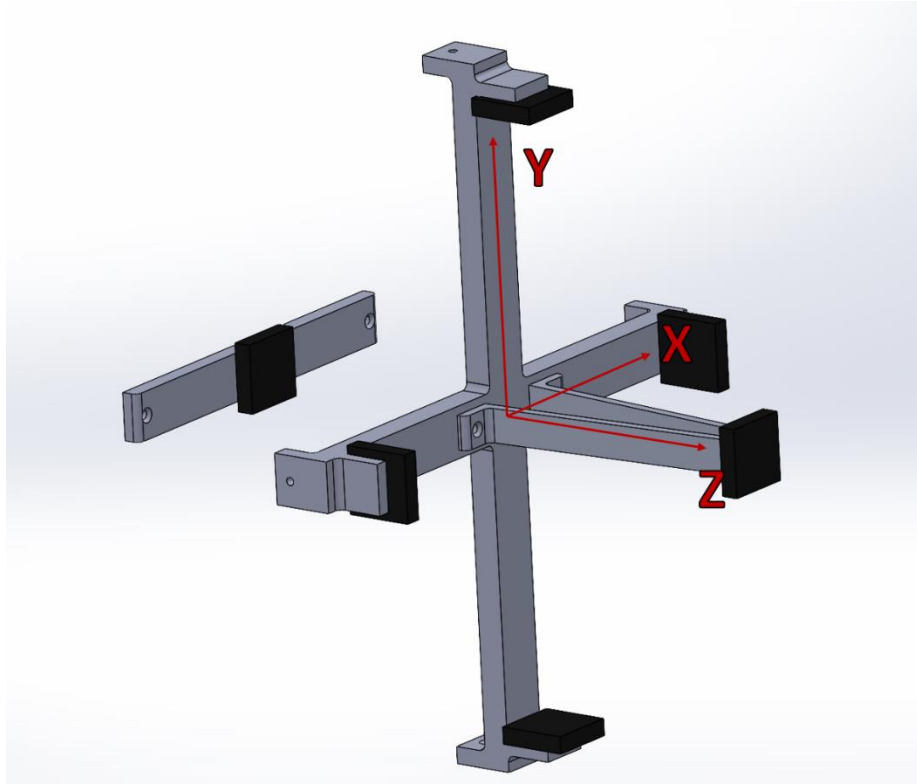


Figure 1.1 Gradiometer Payload with Labeled Axes

In order for the gradiometer to collect accurate data, the axes of the gradiometer must be aligned with the spacecraft's center of mass during the entire science phase. This requires the location of the center of mass to not change as propellant tanks are drained. The locations of propellant tanks were adjusted such that their mass is balanced about the center of the gradiometer. Figure 1.2 shows the position of the center of mass aligned with the gradiometer for both the fully fueled spacecraft and dry mass. The center of mass moves by only 1 mm between configurations.

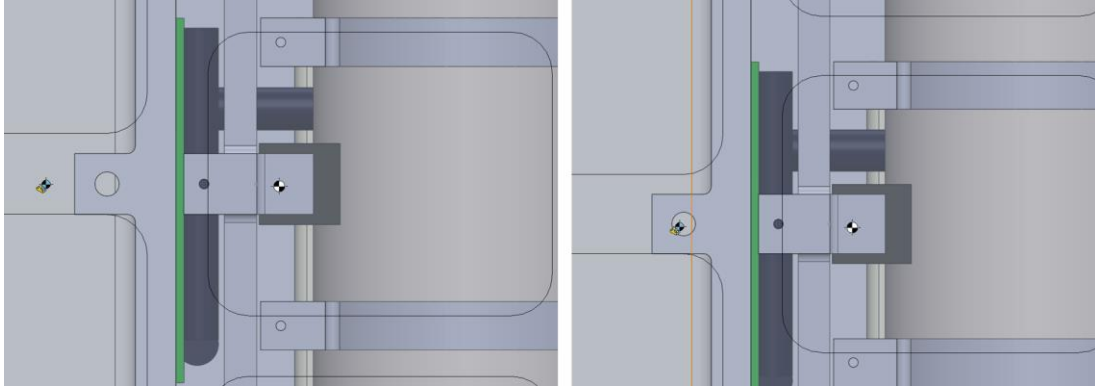


Figure 1.2 Center of mass for fully fueled (left) and dry (right) POGSat

1.7.1. Accelerometer Instrument

The type of accelerometer used is a Micro Electro-Mechanical System (MEMS) Vibrating Beam Accelerometer (VBA). It is a newer type of accelerometer that uses a quartz wafer. As seen below in Figure 1.3, a close-up of the wafer depicts where the seismic mass will vibrate within the decoupling frame and induce a change in resonance to determine the change in acceleration of the sensor.

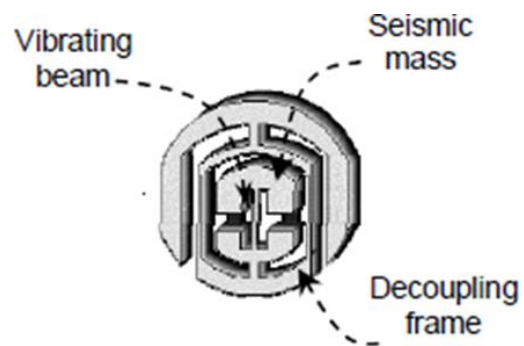


Figure 1.3: Close-Up View of Quartz Wafer [24]

In Figure 1.4, the wafer is shown implemented into resonators and produced into a single sensor.

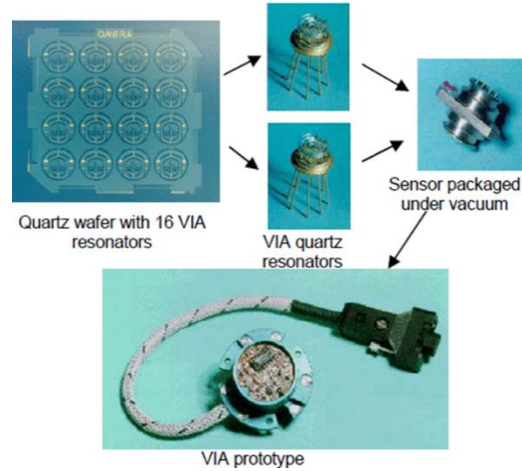


Figure 1.4: Implementation of Quartz Wafer in Sensor [24]

VBA's are predicated using Hooke's Law, which states that the force needed to extend or compress a spring by some distance scales linearly with respect to that distance. In the context of a VBA, a quartz beam acts akin to a spring. The beam has a natural resonant frequency, given by Equation 1.13

$$f = \frac{1}{2\pi} \sqrt{\frac{k}{m}} \quad 1.13$$

where k is the effective spring constant of the beam and m is the seismic mass. When an external acceleration is applied, the seismic mass exerts an additional force on the beam, altering the effective spring constant, and thus the resonant frequency shifts proportionally.

This frequency shift Δf due to acceleration a can be described by Equation 1.14:

$$\Delta f = f_0 \left(1 + \frac{a}{g} \right) \quad 1.14$$

Where f_0 is the resonant frequency at rest, and g is the acceleration due to gravity. The sensitivity of the VBA, defined as the ratio of the frequency shift to acceleration, can be crucial for calibration purposes.

To achieve the high precision necessary for gravimetry, the VBA is encapsulated in a vacuum to minimize damping forces on the beam, such as air resistance, that would otherwise decrease the quality factor Q of the resonator. The quality factor is defined by Equation 1.15:

$$Q = \frac{f_0}{\Delta f_{half-power}} \quad 1.15$$

Where $\Delta f_{half-power}$ is the bandwidth of the resonator at half power. A high Q indicates a sharper resonance peak, allowing for more accurate determination of frequency shifts.

The accelerometer's output stability over time, a key metric of its performance, is assessed by measuring the Allan Deviation, which is used to characterize time-dependent errors in precision oscillators. The Allan Deviation provides insight into the types of noise affecting the VBA and its long-term stability.

In the characterization process on a tilt platform, the device's sensitivity to orientation with respect to gravity is determined, which follows Equation 1.16:

$$S = S_0 \cos(\theta) \quad 1.16$$

With S_0 being the scale factor at zero tilt and θ being the tilt angle. This is vital as it affects the accuracy of the VBA when used in different orientations during the satellite's orbit.

Lastly, temperature effects are accounted for through thermal compensation techniques. As the material properties of the quartz, including the spring constant k and the seismic mass m , are functions of temperature (T), the resonant frequency is also a function of temperature, described by Equation 1.17:

$$f(T) = f_0[1 + \alpha(T - T_0)] \quad 1.17$$

Where α is the temperature coefficient of the resonant frequency, and T_0 is a reference temperature for the sensor.

Compared to GOCE, whose accelerometers had a resolution of 1 mGal, the resolution of a MEMS VBA is suited for gravitational measurements below 10 μ Gal, indicating a defined improvement in the measurement capacity for the payload accelerometers [7], [24].

2. Mechanical Design and Analysis

The structure of the satellite is required to conform to the CubeSat formfactor, and the specifications provided by the satellite deployment mechanism [25]. The satellite structure must also house the payload, propulsion, and electrical components required for the mission. The payload requires a constant center of mass during the science phase, which impacts the location of fuel tanks. A 12U size CubeSat was determined to have sufficient volume for the spacecraft subsystems. The satellite was modeled using SolidWorks, and additional simulations were conducted with Ansys.

2.1. Deployment Mechanism Selection

Due to the standardization of the CubeSat formfactor, there are many deployment mechanisms for CubeSats that can be easily integrated onto a launch vehicle. Most CubeSat deployers interface with the satellite through four rails along the edges of the CubeSat to hold it in place. Alternatively, there are systems which use two tabs that are clamped by the satellite dispenser. Several satellite dispensers were investigated for this mission, shown below in Table 2.1.

Table 2.1: Dispenser Mechanism Selection

Dispenser	Supports 12U	Integration Type	Flight Heritage	Other Features
Canisterized Satellite Dispenser (CSD)	Yes	Tab-Based	Since 2013 (Falcon 9, Electron)	Pre-loaded tabs for accurate vibration modeling
QuadPacks	Yes	Rail-Based	Since 2014 (Falcon 9, Soyuz, Vega)	
Tyvak	Yes	Rail-Based	6U version has heritage since 2016	Isolation system reduces vibration levels
Mercury 12-T	Yes	Tab-Based	No	

After consideration of these dispensers, the Canisterized Satellite Dispenser (CSD) was selected due to its tab-based system that allows for accurate vibrational modeling, and flight heritage on the Electron vehicle. Additionally, Rocket Lab provides a good amount of documentation and CAD models of the CSD. The CSD is shown below in the 3U, 6U, and 12U sizes (Figure 2.1). The dispenser fully encloses the satellite during launch and has a hinged door which opens to deploy the satellite. The back panel of the dispenser is spring loaded, which ejects the satellite once the door is opened [25].

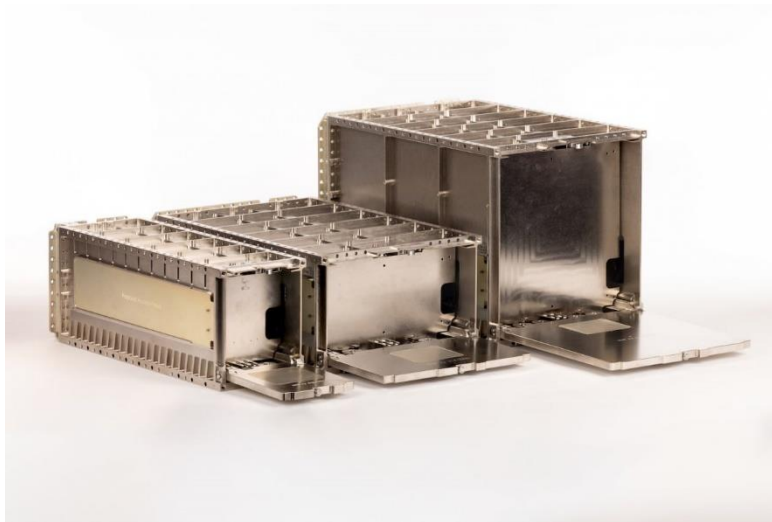


Figure 2.1: The CSD in 3U, 6U, and 12U forms [25]

2.2. Mechanical Requirements

The chosen satellite dispenser imposes several requirements on the properties of the satellite and the response to launch conditions. The key requirements that had to be considered for the mission were the maximum satellite volume, center of mass, tab discontinuities, and tab loading. The CSD datasheet provides maximum dimensions for the satellite volume [26]. To ensure the satellite conformed to these dimensions, a simple model of the maximum satellite volume was created in SolidWorks. The maximum dimensions of the usable payload volume are shown in Figure 2.2. The volume has a depth of 366 mm in the Z direction [26].

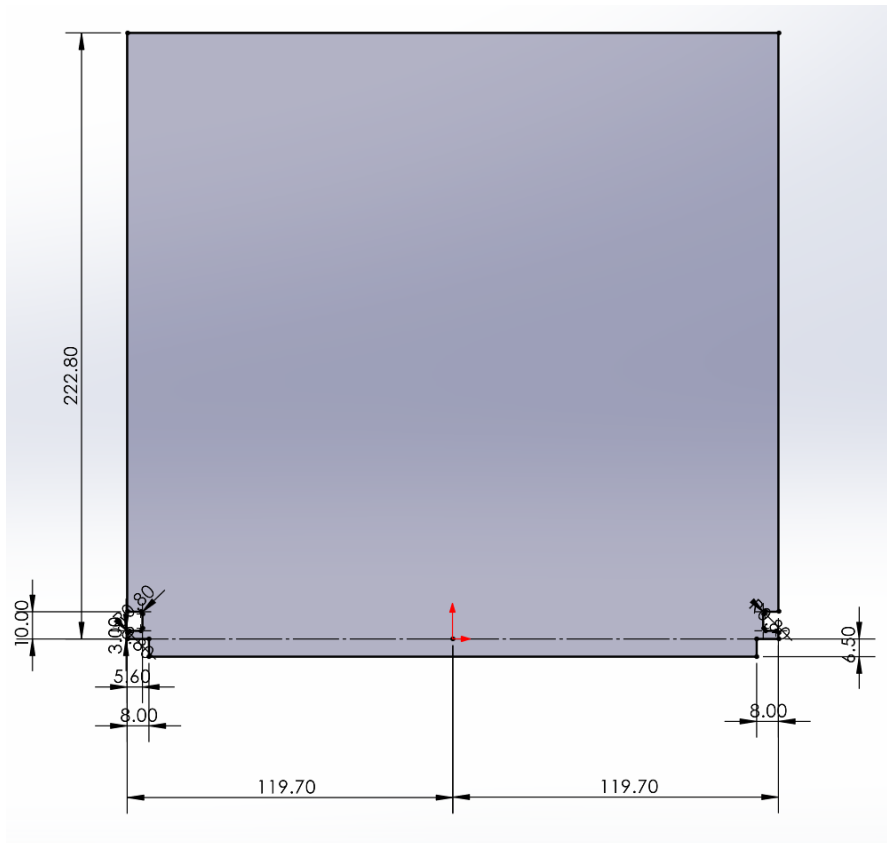


Figure 2.2 Maximum Payload Dimensions [26]

This maximum volume was added as a wireframe to the main satellite assembly to easily see if the bounds were exceeded.

The CSD also provides limitations on the center of mass of the payload while it is stowed. The requirements are shown in Table 2.2.

Table 2.2 Center of Mass Requirements [26]

X-Axis	-40 to 40 mm
Y-Axis	55 to 125 mm
Z-Axis	133 to 233 mm

The stowed center of mass of the satellite was located at (2, 102, 171) mm.

The satellite is required to have tabs running the length of the frame to integrate with the dispenser. The CSD allows for some gaps in these tabs if necessary. The mechanism for articulating our solar arrays requires a small cut to be made in the tabs and bottom of the frame. A maximum gap length of 25 mm is allowed, and the gap must be at least 17.8 mm from the back face of the spacecraft [26]. The gaps in our tabs are only 18 mm and located 18 mm from the back of the frame as shown in Figure 2.3.

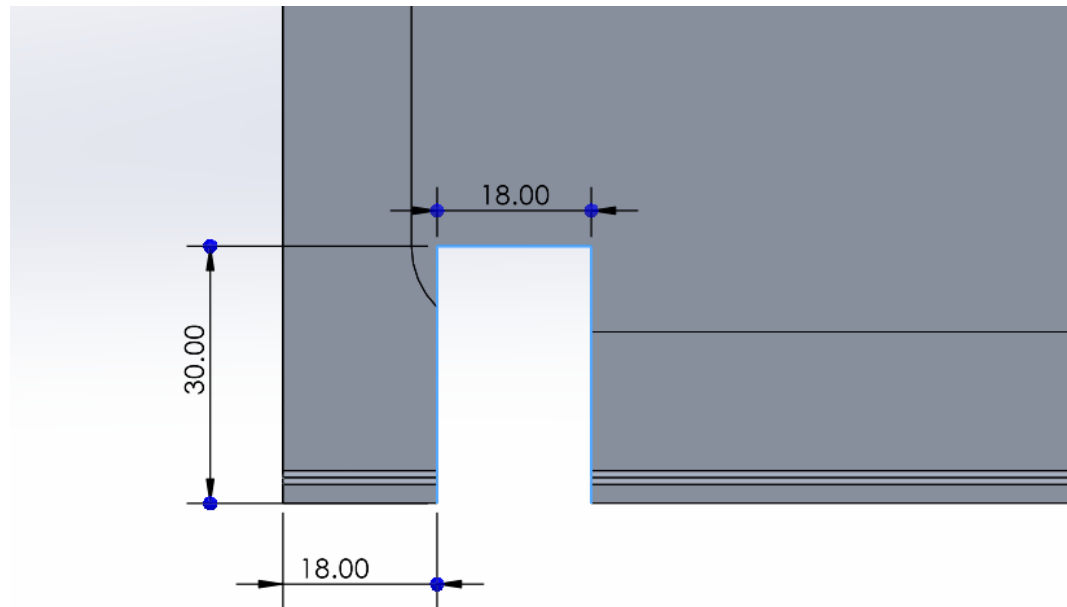


Figure 2.3 View of tab gap in frame side panel

The final requirement of the dispenser is the maximum load force on the tabs during launch. The maximum three-sigma load must be less than 3560N on both tabs to ensure the payload does not slip during launch [26]. This requirement was verified using finite element analysis and is discussed more in Section 2.6.

2.3. Structural Frame

The frame of POGSat provides the primary structure to which internal components are mounted. Due to a lack of availability of 12U frame CAD models, the frame structure was custom designed using SolidWorks to meet the mechanical requirements. The frame was roughly based on the design of the Pumpkin Space 12U Supernova structure [27], with adjustments made to better support different subsystems. The structure must have two tabs running the length of the satellite to be integrated with the CSD. It is made of 6061 Aluminum, as is common for many CubeSat structures. The external frame is shown in Figure 2.4. The satellite also has internal structures to provide mounting surfaces for components such as propellant tanks and electronics. The frame is protected with 0.75 mm of aluminum shielding to limit radiation dose and protect against debris. The space environment is discussed in greater detail in Section 4.

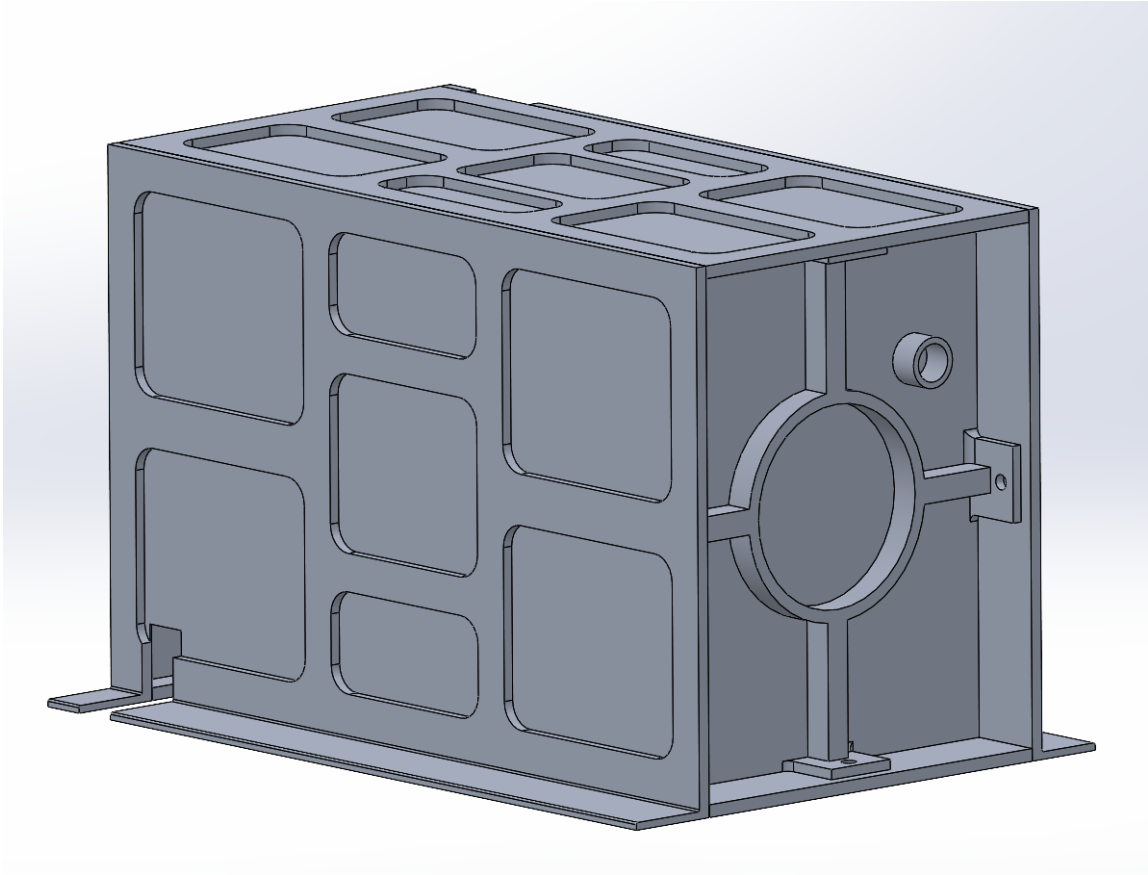


Figure 2.4: POGSat external structure

2.4. Solar Arrays

To provide electrical power to the spacecraft systems, POGSat utilizes deployable solar arrays and body-mounted panels. It was determined by the power subsystem lead that deployable solar arrays would be required to meet the power demands of the spacecraft. These solar arrays must be designed and positioned to maximize the power collected while minimizing drag area. The satellite has two large solar arrays which deploy from opposite corners of the structure. These arrays are oriented to be parallel with the velocity vector to not increase drag. The arrays use a hinged articulation mechanism which allows them to deploy in an accordion-like manner, shown in Figure 2.5. Each side array consists of seven 6U-size solar panels.

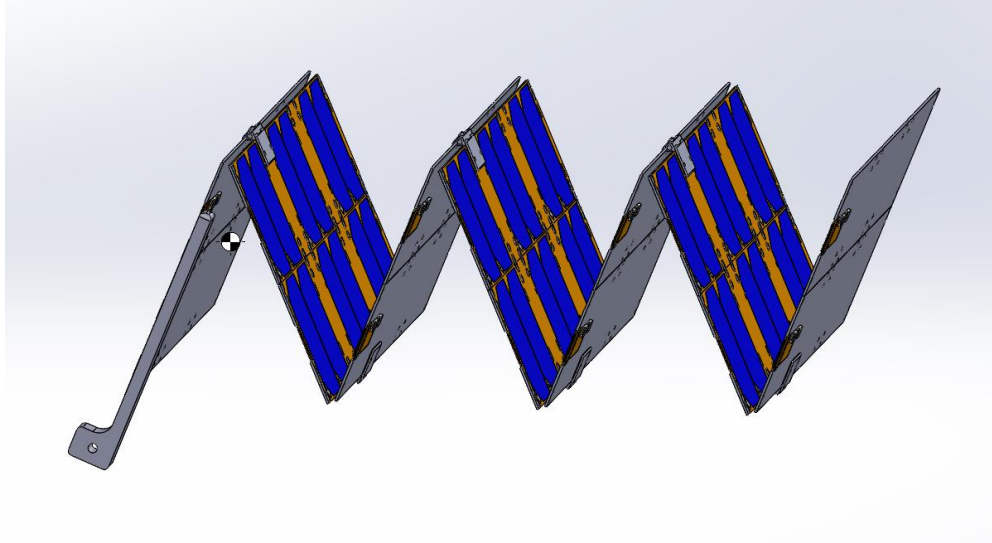


Figure 2.5: Solar array mid-deployment

This arrangement was custom designed to have the number of 6U panels required for our satellite, however it is based on similar folding designs such as the HaWK array from MMA Design [28], and foldable arrays on larger spacecraft.

These solar arrays are mounted on a rotatable structure such that they can articulate to track the sun. The arrays rotate about the Z-Axis of the spacecraft, such that they remain parallel with the velocity vector. The arrays hinge from opposite corners of the spacecraft and will always remain parallel with each other such that their combined center of mass remains in a constant location. Figure 2.6 shows the solar arrays rotated to varying angles, as they will to track the sun throughout the year. Figure 2.7 shows the fully deployed arrays and body mounted panels.

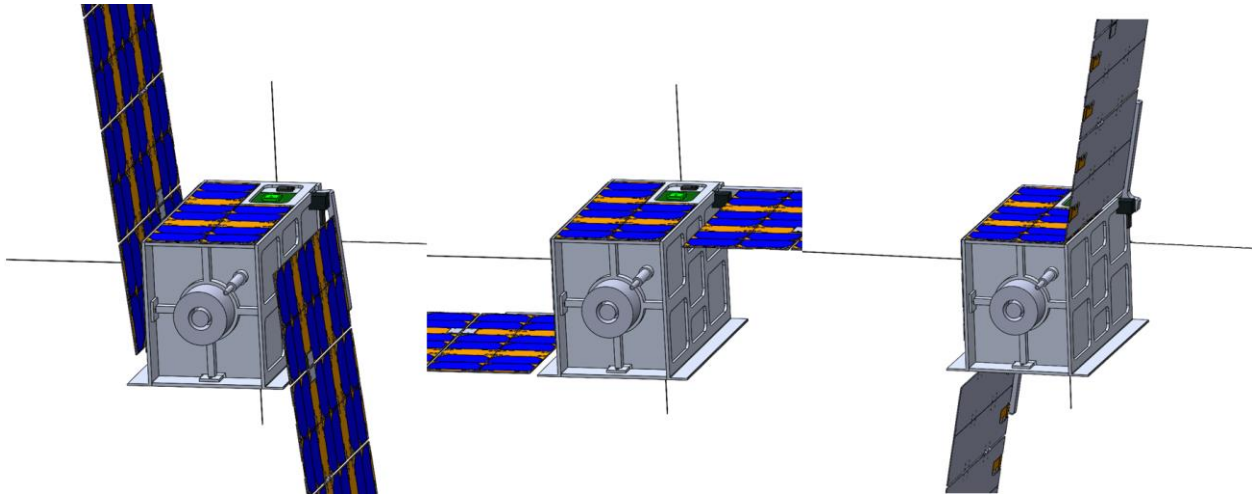


Figure 2.6 Solar arrays at varying angles

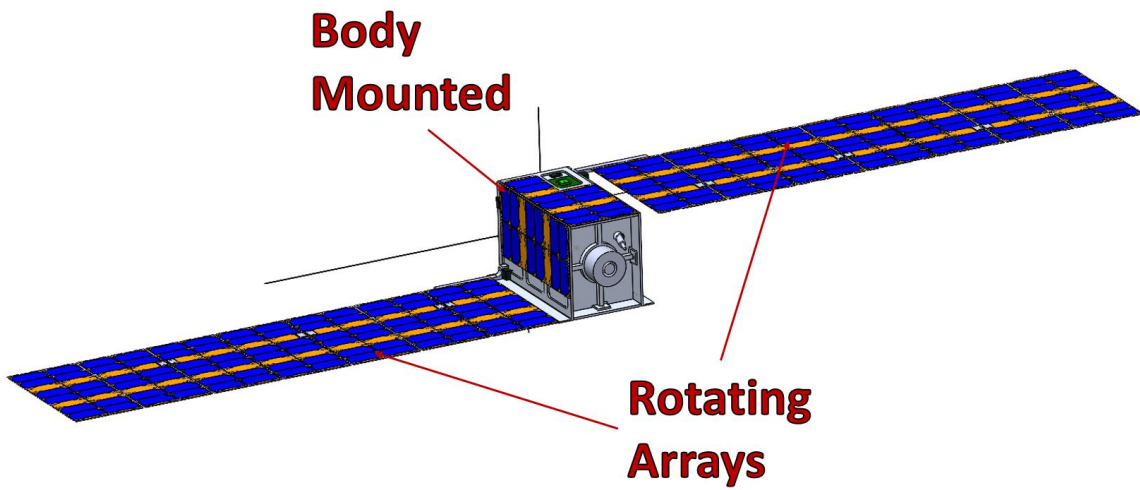


Figure 2.7: Deployed solar arrays

After creating the panel arrangement, a simplified model of the solar panel geometry was made to conduct power simulations. This process involved exporting the CAD model from SolidWorks into

Blender, where the origins of each solar array were defined to allow rotation about the correct axes. The model was exported as a .glTF file, which is used by STK for spacecraft models. A custom metadata file was created to define which surfaces were solar cells and define articulations for the sun tracking panels, as per the process outlined in an AGI tutorial [29]. The power subsystem lead used this model to calculate the power generation in STK [30].

2.5. Subsystem Components

The components required by different subsystems are housed within the spacecraft frame. At the back of the spacecraft is the propulsion system, with the hall thruster and mounting plate. The thruster was positioned such that no components extend past the exit plane of the thruster, as the ionized particles can damage solar cells. Behind the propulsion system is the iodine propellant tank, and the gradiometer payload located at the center of mass. The three magnetorquers are also located near the center of mass. Toward the front of the spacecraft is the two xenon tanks, battery, and electronics stack. Additionally there are two motors for articulating the solar arrays. On the exterior of the frame there are the sun sensors, GPS antenna, and communication antenna. A diagram of the major components is shown in Figure 2.8 and Figure 2.9.

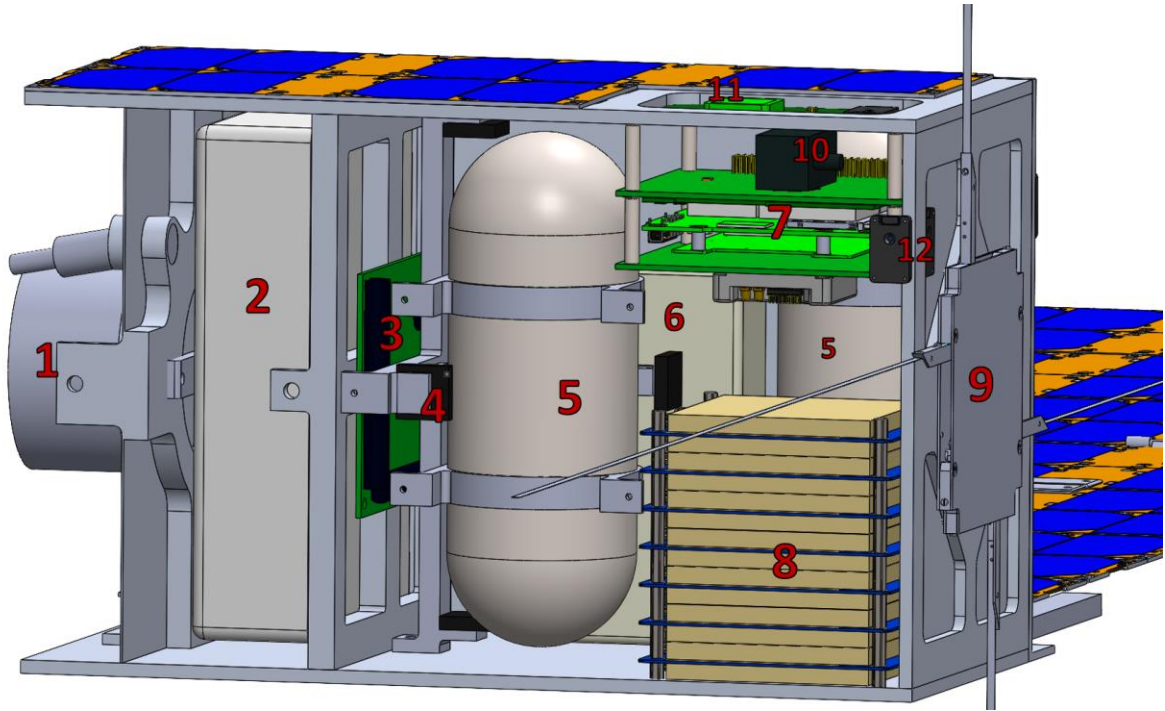


Figure 2.8: Labeled view of internal components

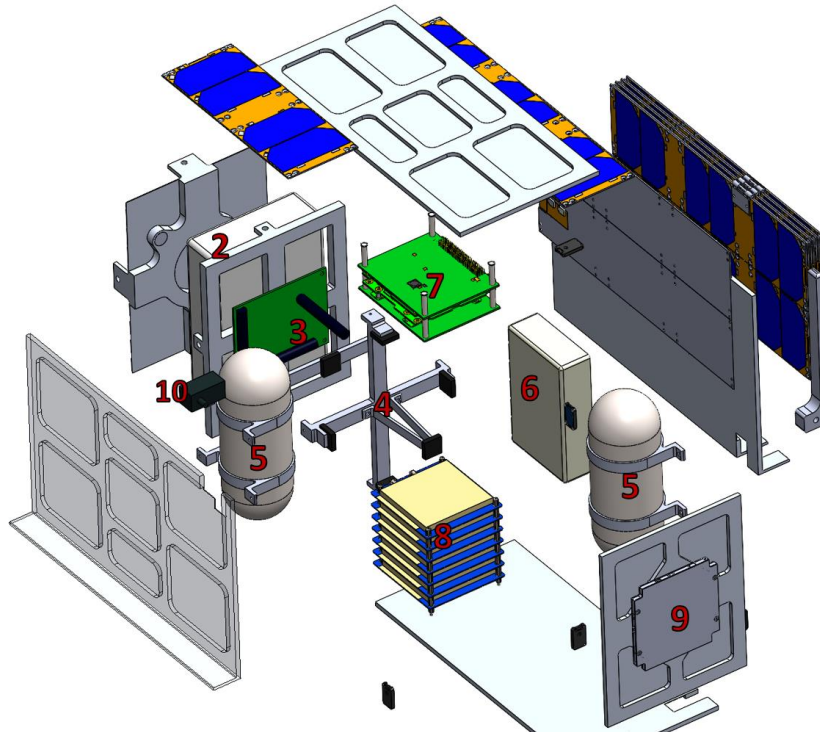


Figure 2.9 Exploded view of components

Number	Component
1	BHT100 Primary thruster
2	Iodine Fuel Tank
3	Magnetorquers
4	Gradiometer
5	Xenon Tanks
6	Propulsion Power Unit
7	Electronics Stack
8	Titan-1 Battery
9	Communication Antenna (Deployed)
10	Solar Array Articulation Motor
11	GPS Patch Antenna
12	Sun Sensors

2.6. Vibration Analysis

Vibration analysis of the satellite was conducted to simulate the loading conditions during launch. The CSD requires that the load force on the tabs must not exceed 3560N during launch [25]. This limit is to prevent the satellite from slipping within the dispenser. To verify the satellite conforms to this requirement, a structural analysis was conducted in ANSYS. A simplified model of the satellite was created to be used for analysis. It consists of only the structural frame, and major components represented as de-featured cuboids. This model reduces the geometric complexity and improves simulation time, while still providing results comparable to the detailed model. Most of the internal components were

modeled as rigid bodies as the intent was to study the vibrations of the satellite as a whole and not individual components. The satellite frame was assigned 6061 Aluminum as its material, and custom materials were made for the other components, with density specified to give the components the correct mass. The analysis required two steps, modal analysis, and random vibration analysis. The model was set up in Ansys Workbench as shown in Figure 2.10.

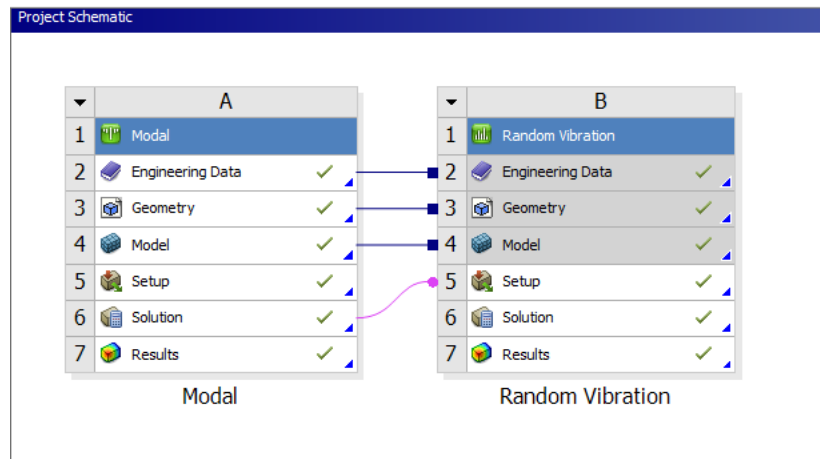


Figure 2.10 Setup of Simulation in Ansys Workbench

With the simplified geometry imported, connections between components were auto-generated by Ansys, and then checked to ensure accuracy. A mesh was created using adaptive sizing with a resolution of 7. The meshed geometry is shown in Figure 2.11.

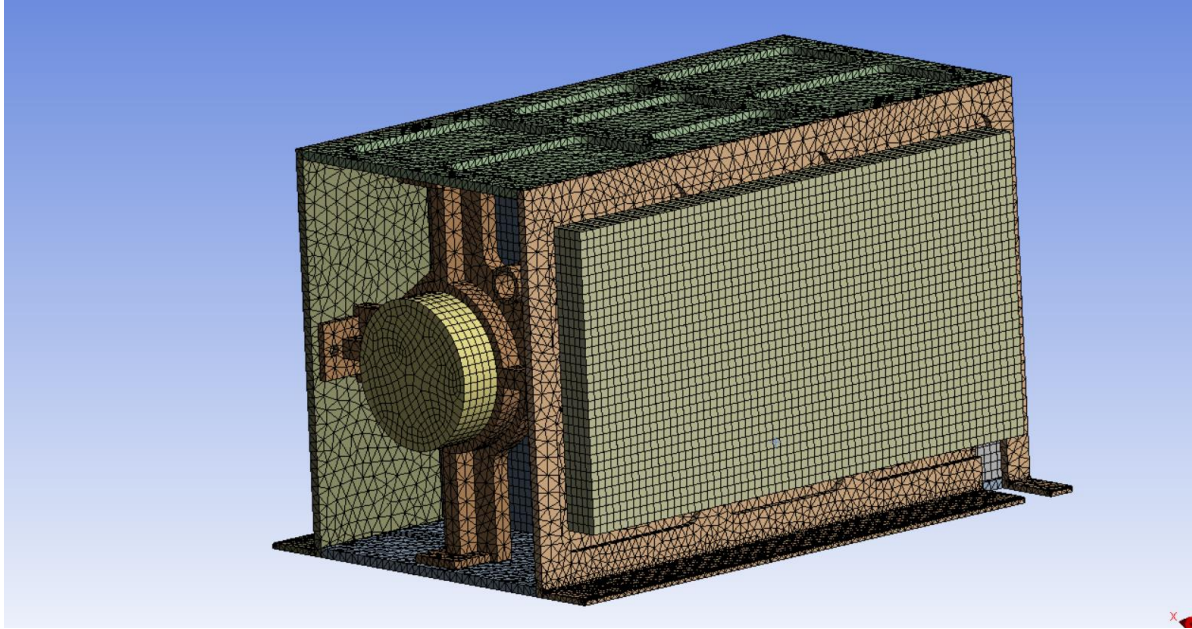


Figure 2.11: Mesh of simulation model

The top surfaces of the tabs of the frame were set as fixed boundary conditions, to represent the clamping of the frame to the CSD. A modal analysis was then conducted to determine the frequencies and shapes of the vibrational modes of the satellite. The CSD Payload Specification guide [26] suggests analyzing the modes from 20 – 2000 Hz. To ensure all relevant modes were found, 30 modes were searched for in the range of 20 – 10000 Hz. The modal analysis was run and frequencies of vibrational modes were found. The vibration modes of the satellite and mode shape are seen in Figure 2.12 and Figure 2.13. The minimum natural frequency was found to be 2360Hz.



Figure 2.12 Satellite Vibration Modes

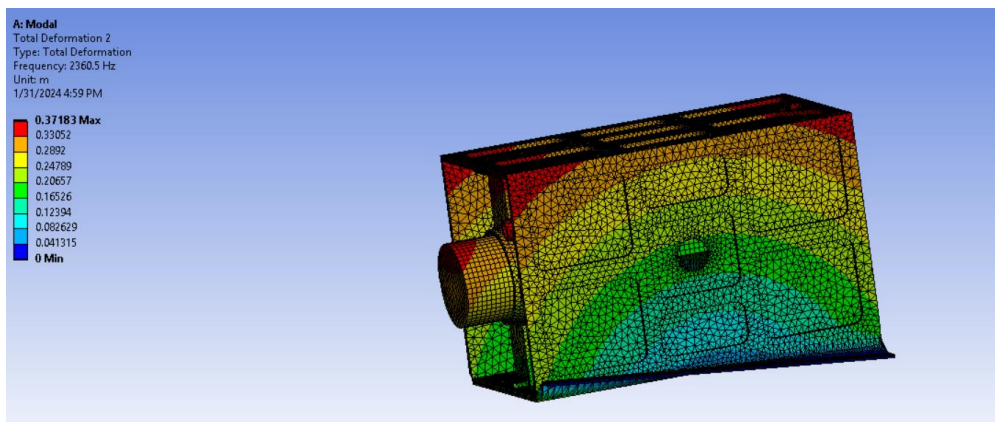


Figure 2.13 First Satellite Mode Shape

With the vibration modes obtained, a random vibration analysis was performed using the Power Spectral Density data from the Electron launch vehicle. The Electron Payload Users Guide provides a PSD curve to use for CubeSat class satellites, as shown in Figure 2.14 [21].

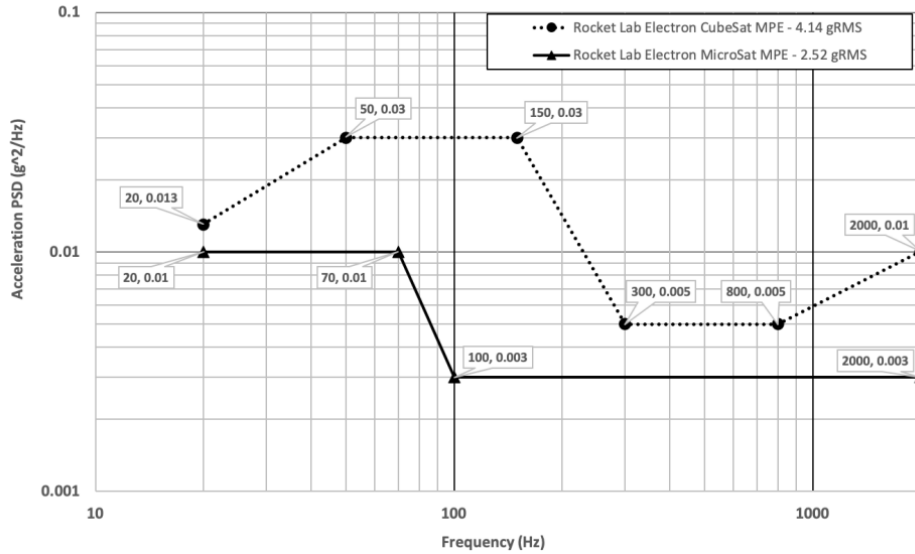


Figure 2.14 Electron PSD Curve [21]

The CubeSat curve was input as a PSD-G acceleration in the vibration analysis module. Three identical PSD accelerations were used, one for each axis. Directional deformation results were retrieved for each axis, as well as a force reaction probe at the tabs. Due to the random nature of the vibration input, the results are given as probabilities. The values used by the CSD specifications are three-sigma values, meaning they represent the maximum force three standard deviations from the mean. The three-sigma

force reaction at the tabs was found to be 3460N, and the maximum deformation was 0.001 mm as seen in Figure 2.15.

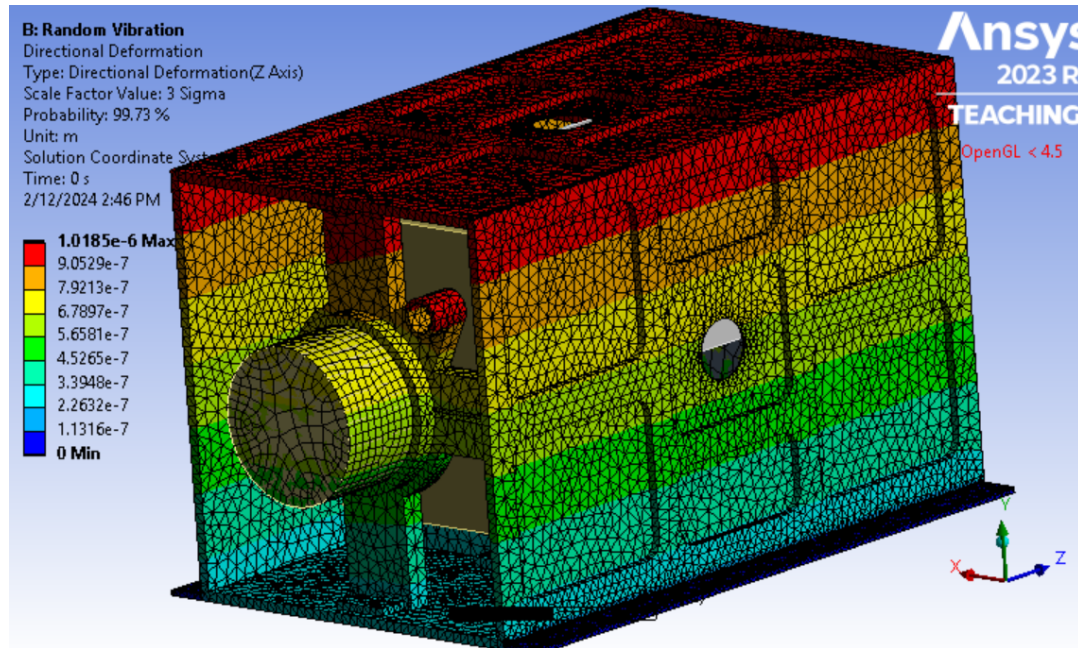


Figure 2.15 Z-Axis Deformation

The CSD datasheet [25] also discusses the use of vibration isolators to reduce accelerations and tab loading. The effects of vibration isolators were briefly investigated, however it proved to be challenging to accurately model, and was ultimately deemed unnecessary.

3. Propulsion

The primary role of the propulsion system is to ensure POGSat is equipped to perform the necessary orbital maneuvers throughout the mission phases. The propulsion system is required to make necessary orbital modifications and perform drag compensation utilizing an onboard propulsion system as well as magnetorquers for attitude control. Magnetorquers were selected for precise control and reorientation and will be primarily used in the Phase Zero detumbling phase and within Phase Two to ensure the payload is oriented towards the Earth. Further detail regarding the attitude control of POGSat is included in the accompanying report [30].

3.1. Types of Propulsion

The primary types of propulsion considered for the mission were chemical and electrical propulsion systems. Each propulsion subtype has its own merits, and a full thruster down select of the Consumer Off the Shelf (COTS) options was used to determine the appropriate propulsion system. A full summary of the propulsion system down select is presented in Appendix A. Chemical propulsion systems, including monopropellant, cold gas, and alternative monopropellant systems, have a categorically higher thrust output, and are ideal for missions with maneuvers that must be completed with a short burn duration [31]. Electrical propulsion systems, including electrospray, Hall effect, and ion systems, have a categorically higher specific impulse and are ideal for missions with maneuvers with that require low thrust and high propulsion efficiency and/or relatively large ΔV .

3.2. Thruster Trade Study

The mission parameters laid out suggested two primary phases of the mission where the primary propulsion system would be utilized: Phase One, which would require a large ΔV to reach the intended altitude needed for data collection, and Phase Two, which requires frequent station-keeping and drag compensation to maintain an eLEO orbit pattern.

3.2.1. Dual-Mode Configuration

The first thruster configuration considered was a dual-mode propulsion system consisting of a chemical monopropellant thruster and electrospray thruster to provide thrust for the separate phases of the mission, with the chemical monopropellant providing thrust for Phase One and an electrospray providing thrust for Phase Two station-keeping. This meant that the thruster configuration would need to minimize total mass and reduce power consumption while suiting the requirements to perform the needed maneuvers. The chemical thruster considered for this model was the BGT-X5 Ascent monopropellant thruster produced by Busek [32]. This thruster stuck out due to its use of Ascent propellant, which has a 45% greater mass density and improved thrust and specific impulse compared to a standard hydrazine thruster. The use of an ionic liquid enables a propulsion model to be constructed with an electric propulsion system compatible with Ascent fuel, reducing the number of unique fuel tanks required. The specifications of the BGT-X5 thruster are presented in Table 3.1.

Table 3.1: BGT-X5 Specifications [32]

Nominal Thrust	0.5 N
Specific Impulse	225 s
System Power	20 W
System Volume	1U
Propellant	Ascent

The electric thruster considered for this dual-mode system was the Scalable ion Electrospray Propulsion System (SiEPS) produced by MIT [33]. This thruster was considered due to the modular configuration and low power required compared to most marketed electrospray thrusters. In addition, the compatibility with Ascent propellant enables a hybrid model to be constructed with the BGT-X5 thruster. The specifications of the integrated SiEPS thruster configuration, composed of eight thrusters, are presented in Table 3.2.

Table 3.2: SiEPS Thruster Characteristics [33]

Nominal Thrust	7.4 μ N
Specific Impulse	1150 s
System Power	6 W
System Volume	0.8U
Propellant	Ascent

The second electric thruster considered for the dual-mode configuration was the Nano Field-emission Electric Propulsion (NanoFEEP) produced by Morpheus Space [34]. This thruster was considered due to the small, modular configuration and low power required compared to most marketed electrospray thrusters. However, the use of liquid Gallium as a propellant source would require the use of two separate fuel tanks, adding system complexity and increasing the overall structural volume required for the propulsion system. The specifications of the integrated NanoFEEP thruster configuration, comprised of four thrusters, are presented in Table 3.3.

Table 3.3: NanoFEEP Thruster Characteristics [34]

Nominal Thrust	16 μ N
Specific Impulse	7000 s
System Power	12 W
System Volume	1U
Propellant	Gallium

3.2.2. Single-Mode Propulsion System

The second thruster configuration considered was a single-mode propulsion system, using only a form of electric propulsion as the primary propulsion system. The thruster considered for this model, the Busek BHT-100 Hall thruster, was considered due to its high thrust compared to many alternate forms of

electric propulsion [35]. To generate the plasma required for system functionality, the BHT-100 is paired with a compatible LaB6 Hollow Cathode [36]. The specifications of the BHT-100 thruster configuration, including the hollow cathode required for plasma generation, are presented in Table 3.4.

Table 3.4: BHT-100 Thruster and LaB6 Cathode Characteristics [35],[36]

Nominal Thrust	0.007 N
BHT-100 Specific Impulse	1000 s
LaB6 Mass Flow Rate	$1 \times 10^{-7} \text{ kg/s}$
Combined System Power	100 W
BHT-100 Volume	0.276 U
LaB6 Cathode Volume	0.0035 U
BHT-100 Propellant	Iodine, Xenon
LaB6 Propellant	Xenon

The second thruster considered for the single-mode propulsion system was the NPT30-12-1U from ThrustMe, which was considered due to its higher Isp and lower power draw than the BHT-100 [37]. This thruster would minimize the amount of onboard mass required for station-keeping, at the expense of a longer Phase One maneuver duration. The specifications of the NPT30-12-1U are presented in Table 3.5.

Table 3.5: NPT30-12-1U Thruster Characteristics [37]

Nominal Thrust	0.0011 N
Specific Impulse	2400 s
System Power	65 W
System Volume	1U
Propellant	Iodine

A full list of the considered thrusters and their performance specifications can be found in Appendix A.

3.3. Preliminary Phase One Orbital Analysis

To assist in determining the ideal thruster configuration for POGSat, initial ΔV and propellant mass fraction estimates were made using a MATLAB script in Appendix B and Appendix C. These estimates were to help understand the performance and capabilities of the thrusters as well as quantify the amount of thrust necessary to complete the initial transfer in Phase One while reserving propellant for Phase Two, the predicted ΔV -intensive phase of the mission. The MATLAB script uses the initial and final altitudes from an expected Electron ejection, assuming an ideal launch at the ideal inclination. For a preliminary analysis, propellant mass was calculated with the maximum allowable mass for a 12U CubeSat to ensure POGSat can complete the mission with sufficient propellant onboard. For the case of the chemical monopropellant system, this analysis was modeled as a Hohmann transfer, detailed in Appendix B. The driving equation for a Hohmann Transfer is listed in Equation 3.1:

$$\Delta V = \sqrt{2\mu_E \left(\frac{1}{r_0} - \frac{1}{\Delta A + r_0} \right)} - \sqrt{\frac{\mu_E}{r_0}} + \sqrt{\frac{\mu_E}{\Delta A + r_0}} - \sqrt{2\mu_E \left(\frac{1}{\Delta A + r_0} - \frac{1}{\Delta A + 2r_0} \right)} \quad 3.1$$

where ΔA is the altitude change in km, r_0 is the initial radius upon ejection from the CSD, and μ_E is the standard gravitational parameter of Earth.

For the electric propulsion systems, the analysis was performed using the Edelbaum equation for a spiral trajectory, shown in Equation 3.2, which is best suited for low-thrust trajectories:

$$\Delta V = \sqrt{V_i^2 + V_f^2 - 2V_i V_f \cos(\Delta i)} \quad 3.2$$

ΔV is the required change in velocity to complete the phase change in meters per second, V_i and V_f are the velocities on the initial and final circular orbits in meters per second, and Δi is the required inclination

change in radians. The MATLAB code associated with the electric propulsion systems is detailed in Appendix C.

Once the ΔV was found, it can be used in the Rocket Equation, shown in Equation 3.3:

$$\Delta V = g I_{sp} \ln \left(\frac{m_i}{m_f} \right) \quad 3.3$$

where ΔV is the total ΔV needed for the maneuver, m_f is the mass of the CubeSat after the burn in kg, m_i is the mass of the CubeSat before the burn in kg, g is the acceleration of gravity, and the I_{sp} is provided by the thruster manufacturer in seconds. From Equation 3.3, the propellant mass ratio for Phase One can be derived and calculated using Equations 3.4 and 3.5:

$$m_p = \left(1 - \frac{m_f}{m_i} \right) m_i \quad 3.4$$

$$\frac{m_p}{m_i} = \left(1 - \frac{m_f}{m_i} \right) \quad 3.5$$

where m_p is the mass of the propellant consumed within the maneuver burn in kg. This ratio measures the approximate percent of the CubeSat that will need to be composed of propellant to complete the maneuver.

The burn duration for the Phase One maneuvers can be found using Equation 3.6:

$$t_b = \frac{m_p g I_{sp}}{T} \quad 3.6$$

where t_b is the burn time required for the maneuver and T is the thrust provided by the thruster in Newtons.

Using the BGT-X5 as a benchmark with the standard 24 kg mass limit of a 12U CubeSat, the calculated propellant mass fraction, $\frac{m_p}{m_i}$, is 0.0599, provided an ideal deployment at the correct inclination. This mass fraction is not suitable, as it presents a required volume of 0.965 U which leaves minimal additional volume for station-keeping maneuvers. While this confirmed that the mission was feasible, additional thrusters were considered to ensure a maximum lifespan. Each thruster is assumed to be using the densest propellant to conserve internal volume. The results of the trade study using the thrusters detailed in Section 3.2 are tabulated in Table 3.6.

Table 3.6: Thruster Trade Study Results

Thruster	Thrust (N)	I_{sp} (s)	Power (W)	$\frac{m_p}{m_i}$	Burn Time (days)	Volume (U)
BGT-X5	0.5	225	20	0.060	0.073	0.965
SiEPS (integrated)	7.4×10^{-5}	1717	6	0.004	256.589	0.065
NanoFEEP	16×10^{-5}	7000	12	0.001	118.854	0.004
BHT-100	0.007	1000	100	0.007	2.708	0.034
NPT30-12-1U	0.0011	2400	65	0.003	17.271	0.014

3.4. Propulsion System Selection and Design

Based on the initial analysis presented in section 7.3, Busek's BHT-100 Hall Thruster was selected as the primary propulsion system for POGSat. The BHT-100 presents the minimum maneuver time with the lowest propellant mass fraction and internal volume relative to maneuver duration. While the other electric propulsion options reserve more volume for further station-keeping in Phase Two, the

short maneuver duration extends the duration of Phase Two data collection while reducing additional required cathode propellant.

3.4.1. Propellant Feed System Design

To accommodate a propulsion system that requires the use of a temperature-controlled substance, the propellant feed system for POGSat must be able to regulate its temperature and pressure to ensure even sublimation of the Iodine and prevent condensation along the feed lines [38]. For Iodine to be utilized as a propellant, the tank and feed lines must be kept at 100° C, facilitated using thin-film Kapton® heat strips applied to the main propellant tank and feed lines that route the tank to the anode of the thruster [39]. An INCONEL® X-750 filter is applied to prevent Iodine granules from entering the body of the feed system, selected for its high heat resistance and usage in laboratory testing of Iodine feed systems [40, 41]. VACCO Industries latch valves are placed after the filters to ensure that the reservoirs are isolated from the main feed system until operation, with the high- and low-pressure models used for the Xenon and Iodine tanks, respectively [42, 43]. This ensures that Iodine or Xenon does not enter the system when the spacecraft is awaiting ejection within the CSD. Platinum thin-film (PTF) Temperature sensors are also placed at key junctions of the feed lines, including the propellant tank, the interface between the feed line and latch valve, and the interface between the propellant line and the discharge channel [44, 45]. A PTF temperature sensor was selected due to its high accuracy and small form factor, allowing multiple locations along the feedline to be measured for consistent temperature. Internal temperature and pressure of the system is maintained using a VACCO Industries pressure flow control valves (PFCVs) with integrated thermistors to ensure the Iodine is kept at a consistent temperature and pressure [38]. The VACCO Industries PFCV was selected due to its integrated thermistor, which allows for a variable flow rate while introducing fewer breaks in the feedline for a separate thermal controller. A simplified block diagram representing the propellant feed scheme is shown in Figure 3.1, and a table of required components is listed in Table 3.7.

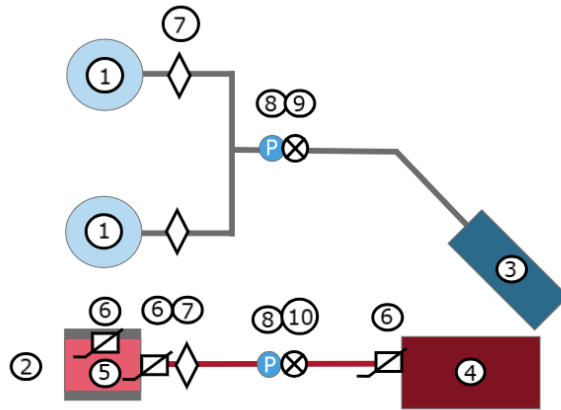


Figure 3.1: POGSat Propellant Feed Scheme

Table 3.7: POGSat Propellant Feed Scheme Component List

Number	Component
1	Xenon Storage Tank
2	Iodine Storage Tank
3	LaB6 Hollow Cathode
4	BHT-100 Thruster
5	Kapton® Heat Strips
6	PTF Temperature Sensor
7	INCONEL® X-750 filter
8	VACCO Industries PFCV
9	VACCO Industries High Pressure Latch Valve
10	VACCO Industries Low Pressure Latch Valve

3.5. Orbital Analysis

Once the primary propulsion system was selected, the amount of propellant and accurate burn durations could be determined accurately utilizing System Tool Kit's (STK) Astrogator to conduct an in-depth orbital analysis using a low-thrust, finite maneuver. This would present an accurate representation of the propellant required to perform the initial maneuver, the altitude lowering from the deployment altitude of 500 km to the target altitude of 260 km, while factoring in atmospheric drag and a modified burn pattern.

To maximize the battery lifetime, the BHT-100 thruster can only fire while the POGSat solar array is within the full sun portion of the orbit. Further details regarding the power generation and management over the course of a mission are included in the accompanying report.

3.5.1. Preliminary Lifetime Analysis without Station-keeping

Using STK's Astrogator tool, a Mission Control Sequence (MCS) was created to accurately model the orbit lowering required to reach the target altitude of 260 km. Using a series of automatic sequences housed within a propagate segment that reference the solar incidence angle of POGSat and ensure a finite burn maneuver is only incited when in full sun, an accurate model was constructed that detailed the necessary burn patterns and thrust profile presented by the BHT-100, depicted in Figure 3.2.

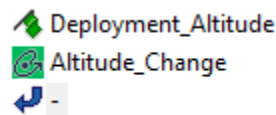


Figure 3.2: Finite Altitude Lowering Maneuver MCS

To reflect the modified burn pattern imposed by the power subsystem, an automatic sequence was developed to ensure that the BHT-100 thruster was only firing while the POGSat solar array was in full sun. The sequence begins when the solar panels come into full view of the sun, which initiates a finite burn with the BHT-100 thruster to begin lowering the altitude of the POGSat. When the solar panels leave full sun, beginning the eclipse phase of the orbit, the automatic sequence halts the burn until the solar

panels enter full sun. This burn structure was implemented into the automatic sequence, as shown in Figure 3.3.

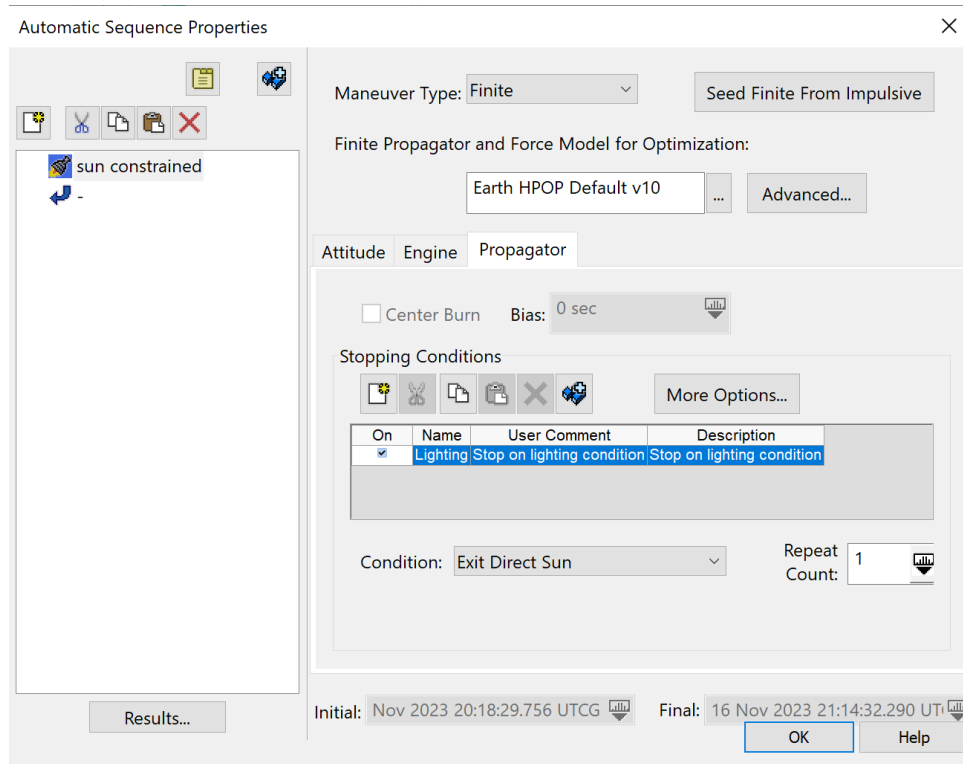


Figure 3.3: Automatic Sequence Required for Full-Sunlight Burn Constraint

This maneuver had a burn time of 2.698 days and required 0.166 kg of Iodine as well as 0.023 kg of Xenon to complete. The entire duration, including periods where the BHT-100 is not firing, is 4.24 days. To determine the duration POGSat can maintain an altitude band of between 280 and 240 km, the STK Lifetime Analysis tool can be used to estimate the decay rate of POGSat provided established initial conditions including drag area, spacecraft mass, and altitude. The lifespan differences between the two inclinations vary due to the atmospheric conditions present within the desired inclination. Due to the inherent differences present between the two inclinations, as a worst-case estimate, total lifespan will be determined by the shorter lifespan of the two presented inclinations, as shown in Figure 3.4 and Figure 3.5. The shorter of these two lifespans dictated the POGSat mission lifespan, shown in Figure 3.4.

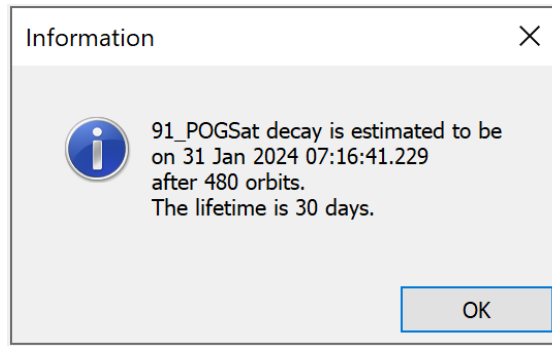


Figure 3.4: STK Lifetime Analysis Tool estimate for altitude decay at 91° inclination

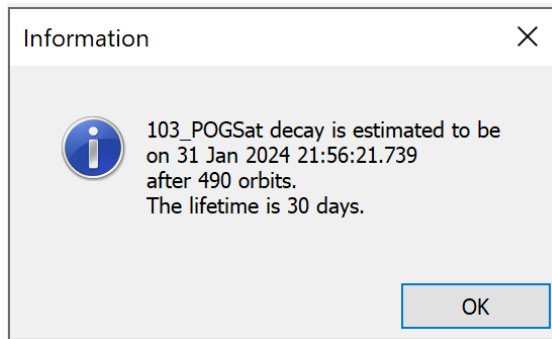


Figure 3.5: STK Lifetime Analysis Tool estimate for altitude decay at 103° inclination

The Lifetime Analysis tool was also utilized to determine the duration of time required to successfully deorbit. To ensure that POGSat can successfully reach a final burnout altitude of 75 km in a worst-case scenario, the deorbit duration was taken at the target altitude of the POGSat with the inclination with a longer lifespan, 91°. These results are displayed in Figure 3.6.

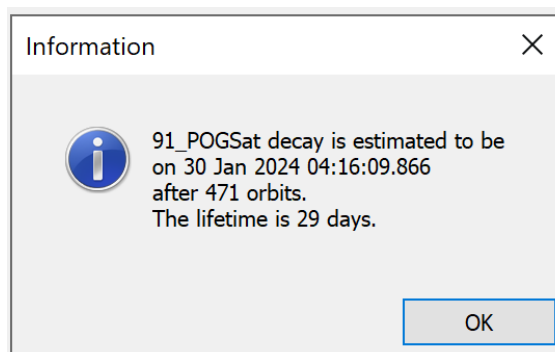


Figure 3.6: STK Lifetime Analysis Tool estimate for Deorbiting at 91° inclination

A summary of the mission timeline and maneuvers are tabulated in Table 3.8.

Table 3.8: Propulsion System maneuver timeline without station-keeping

Maneuver	Initial Altitude (km)	Final Altitude (km)	Burn Time per Maneuver (days)	Iodine m_p required (kg)	Xenon m_p required (kg)	ΔV Required ($\frac{km}{s}$)	Lifetime Duration (days)
Phase 1 Orbit Lowering	500	260	2.70	0.19	0.12	0.13	4.24
Phase 2 Without Station-keeping	260	210	-	-	-	-	30.54
Phase 3 Deorbit	260	75	-	-	-	0.05	28 – 29
Total			2.70	0.19	0.12	0.18	62.78

Due to the significant altitude degradation as a result of the atmospheric density and drag area, station-keeping maneuvers are required to ensure mission longevity.

3.5.2. Preliminary Lifetime Analysis with Station-keeping

Due to the significant drag presented due to atmospheric density at eLEO altitude, station-keeping is a required aspect of the POGSat mission structure. To incorporate station keeping, as well as determine the additional propellant masses required to extend the mission lifespan. An iterative process was taken at a variety of decay altitudes to determine the minimum propellant required to perform repeated station-keeping maneuvers. A lifetime duration can be calculated using the required propellant mass as a constraint. The amount of additional mass is primarily reliant on the internal volume available on each POGSat, with additional focus placed on the overall wet mass of each POGSat to ensure the satellite met the required tab-loading specifications. By dividing the desired lifetime by the decay period presented at each decay altitude, an approximate number of station-keeping burns can be determined. As such, the

lifetime is determined by the amount maximum number of years of station-keeping maneuvers can be performed before running out of fuel. A mission timeline and maneuver summary with the inclusion station-keeping is tabulated below in Table 3.9.

Table 3.9: Propulsion System maneuver timeline with station-keeping

Maneuver	Initial Altitude (km)	Final Altitude (km)	Total Burn Duration (days)	Iodine m_p required (kg)	Xenon m_p required (kg)	ΔV Required ($\frac{km}{s}$)	Lifetime Duration (years)
Phase 1 Orbit Lowering	500	280	2.70	0.19	0.12	0.13	0.01
Phase 2 With Repeated Station-keeping	260	210	396.10	5.14	3.29	3.07	10
Phase 3 Deorbit	260	75	-	-	-	0.05	0.04 - 0.19
Total			398.80	5.33	3.41	3.25	10.06

Each station-keeping maneuver is structured to occur when the altitude of POGSat reaches 210 km, which triggers an automatic sequence to restore the altitude to the desired 260 km circular orbit. In a similar manner to the Phase 1 maneuver, the burns are structured such that they only occur while the POGSat solar panels are in full sun to optimize the battery charge. The decay altitude of 210 km was selected to maximize the lifetime of the orbit without station-keeping, thus decreasing the amount of required station-keeping burns, as well as limiting the eccentricity of the orbit as it decays. By limiting the orbit eccentricity such that the altitude only changes by 50 km, the resultant geoid remains a consistent height [46].

3.5.3. Recommendations and Mission Considerations

While the current propellant mass budget required for 10 years of operation fits within the 12U form factor, there are still methods to optimize the mass budget by utilizing the solar panel arrays as lifting surfaces. Given the nonzero atmospheric density presented at eLEO orbit, a solar panel placed at an angle of attack parallel to the velocity vector would potentially generate enough lift to elongate the lifespan of Phase 2 without station-keeping, depending on the selected altitude and satellite geometry [47]. This would decrease the number of station-keeping maneuvers required to sustain a 10-year mission, thus decreasing the propellant mass required.

4. Environmental Analysis

A critical component of ensuring functionality while in space is accounting for solar and environmental radiation throughout the duration of a mission. The POGSat mission takes place at an operational altitude of 260 km, which places the POGSats within the thermosphere, a layer of the atmosphere that shields the Earth's surface from most of the high energy particle and radiation dosages present from external bodies [48]. As such, the POGSats are exposed to a high dose of radiation that will cause heavy degradation to the internal components unless properly shielded.

4.1. Analysis of Radiation Effects and Design Considerations

To ensure that the internal components were sufficiently shielded within an operational lifespan of 20 years, a maximum accumulated radiation was selected based on the minimum radiation tolerance established by the onboard instruments, tabulated below in Table 4.1.

Table 4.1: Acceptable Radiation Dosage (krad) for Internal Hardware

Component	Acceptable Radiation Dose (krad)
Accelerometers (Backup)	10
Gyroscope	10
Magnetometer	10
UHF Antenna	10
UHF Radio	10
Battery	15
GPS Antennas	15
Iridium Antenna	15
EPS Board	20
Flight Control System	20
Iridium Radio	20
Magnetorquer	20
Fine Sun Sensors	20
Payload Accelerometers	25
Tracking and Telemetry	30

Based on the onboard instrumentation, the shielding would have to ensure that the accumulated radiation could only reach 10 krad within an extended 20-year lifespan.

To provide an expected radiation dosage based on the relative position of the POGSats, STK's Space Environments and Effects Tool (SEET) program could be used to illustrate the accumulated radiation with simulated shielding at a variety of thicknesses. In addition, varying solar activity could be accounted for by setting the simulation to reflect a "Solar Max", representing greater than average solar activity and applying a buffer to the shielding thickness selected. Due to the positioning relative to the Van Allen radiation belt, the 103° inclination POGSat was selected to represent the worst-case shielding required to suit the mission requirements [49]. The yearly accumulated radiation dosage for the 103° inclination POGSat using a variety of thicknesses of aluminized mylar shielding over the course of 20 years is represented in Figure 4.1.

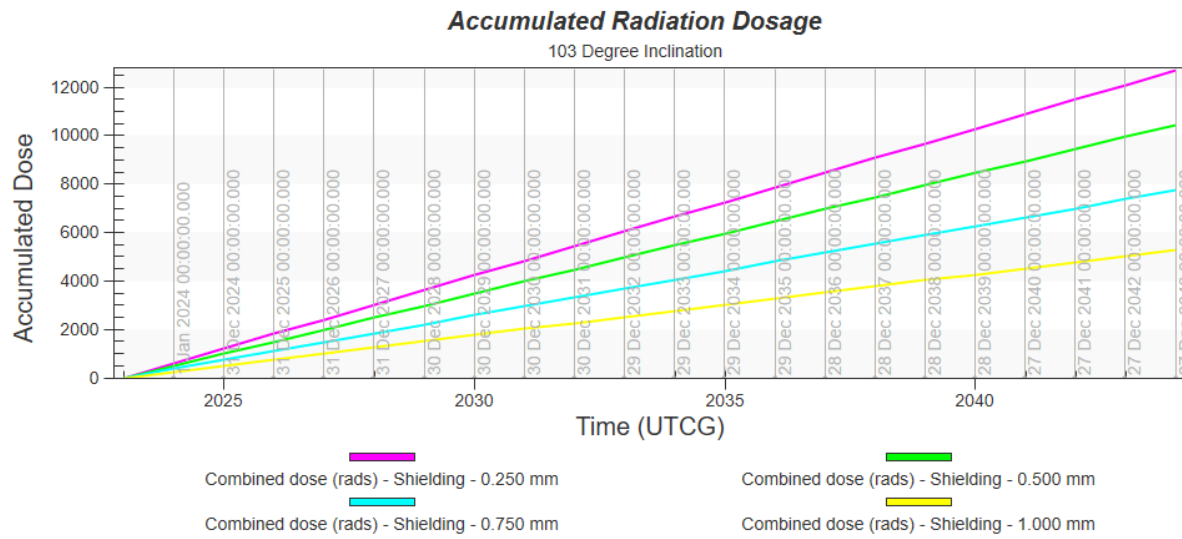


Figure 4.1: STK SEET simulation of total accumulated radiation (rad) using aluminized mylar thicknesses of 0.25, 0.5, 0.75, and 1 mm

Based on the 10 krad acceptable radiation limit, 0.75 mm aluminized mylar shielding ensures that the 103° inclination POGSat only accumulated 7.38 krad of radiation. While 0.5, 0.75, and 1 mm ensures that the internal hardware would resist radiation hardening provided any additional solar activity, with accumulated radiation dosages of 9.91, 7.38, and 5.02 krad, respectively, shielding thinner than 0.5 mm exceeds the 10 krad radiation limit. The shielding thickness of 0.75 mm was selected due to providing the most shielding for the least additional dry mass.

In addition, Solar Energetic Particles (SEPs), corresponding to the level of solar activity present in the mission lifetime, places POGSat at risk for damage. STK®’s SEET tool uses the ESP model to assess the probability of experiencing SEPs at a variety of fluences from 1-100 MeV, factoring in the potential for a worst-case fluence [50]. The ESP model suggests that POGSat will 100% encounter damaging SEPs over the course of the mission; however, the inclusion of the aluminum shielding will block most of the dangerous particles from affecting the internal hardware. The probability of encountering damaging SEPs decreases with higher fluences, which lessens the potential for damaging

impact. The probability of SEP impact for a variety of fluences for both the 91° and 103°, respectively, are presented in Figure 4.2 and Figure 4.3.

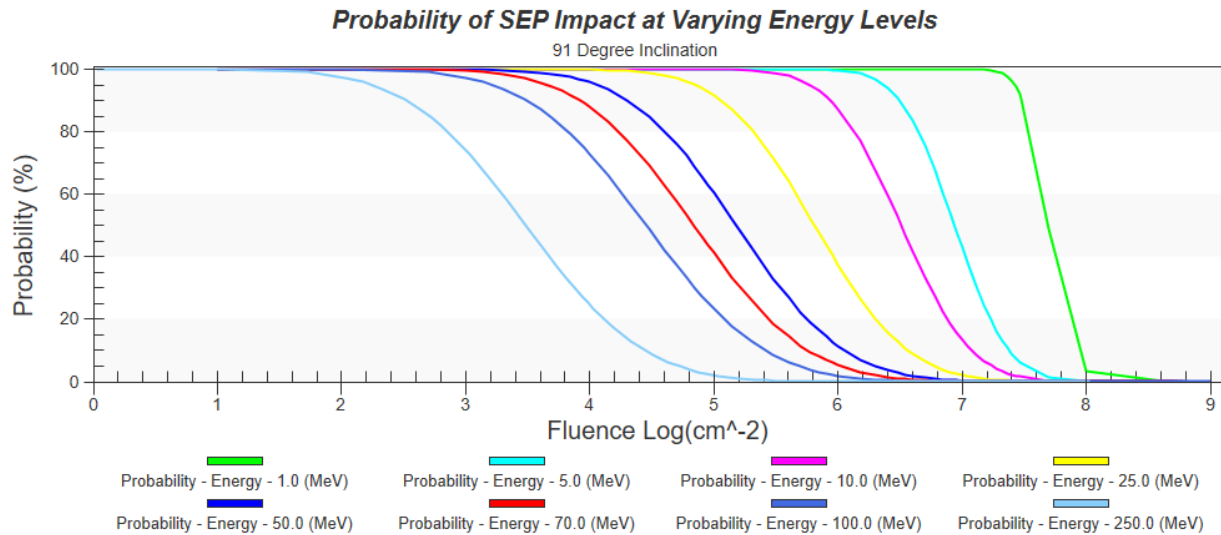


Figure 4.2: STK SEET Simulation of SEP Impact at Varying Energy Levels at 91° inclination

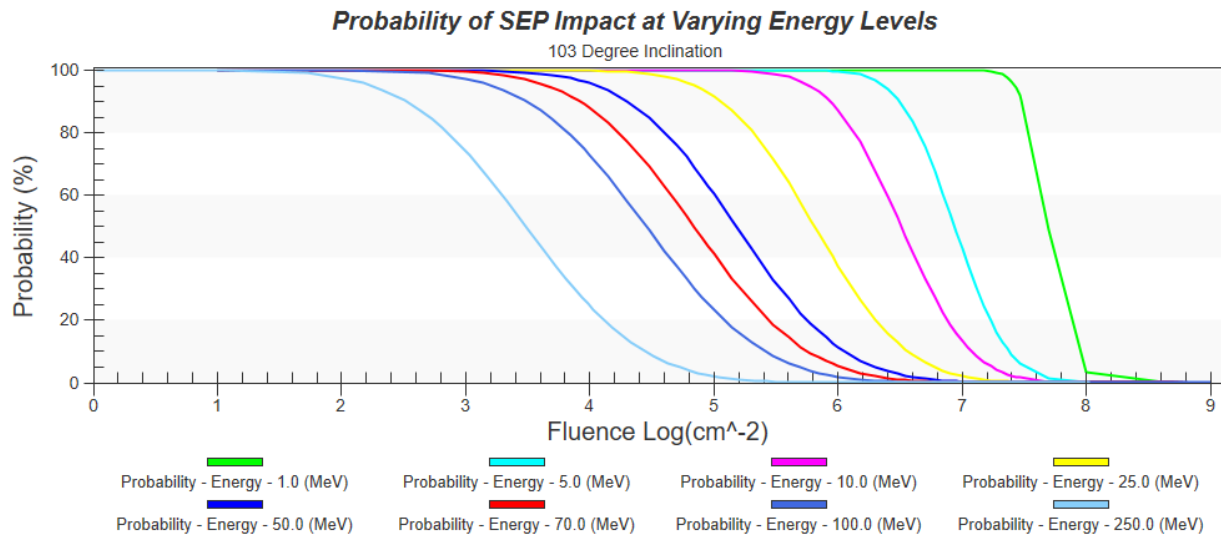


Figure 4.3: STK SEET Simulation of SEP Impact at Varying Energy Levels at 103° inclination

4.2. Analysis of Micrometeorite Effects and Design Considerations

To account for the debris and particle fields around the Earth, it is necessary to model the probability of debris collisions over the expected lifespan of POGSat within the operational altitude. This

was performed using STK®’s SEET tool, which is based on Kessler’s equations (1989) for particle flux provided the orbital position and solar activity from the past 13 months [50]. The cross-sectional area used was POGSat’s 3U x 2U face, representing the largest target area on the CubeSat bus. The analysis performed utilized aluminized mylar, wherein a damaging particle was classified as any particulate matter that penetrates the 0.75 mm radiation shielding over the extended mission lifespan of 15 years. As shown in Figure 4.4 and Figure 4.5, there are no instances where the impact flux overlaps into the damaging impact flux at either the 91° or 103° inclination, respectively. This indicates that over a 20-year lifespan the POGSats will not experience nominal micrometeoroid impact that penetrates the 0.75 mm shielding. The maximum impact flux across both the 91° and 103° inclination is tabulated in Table 4.2.

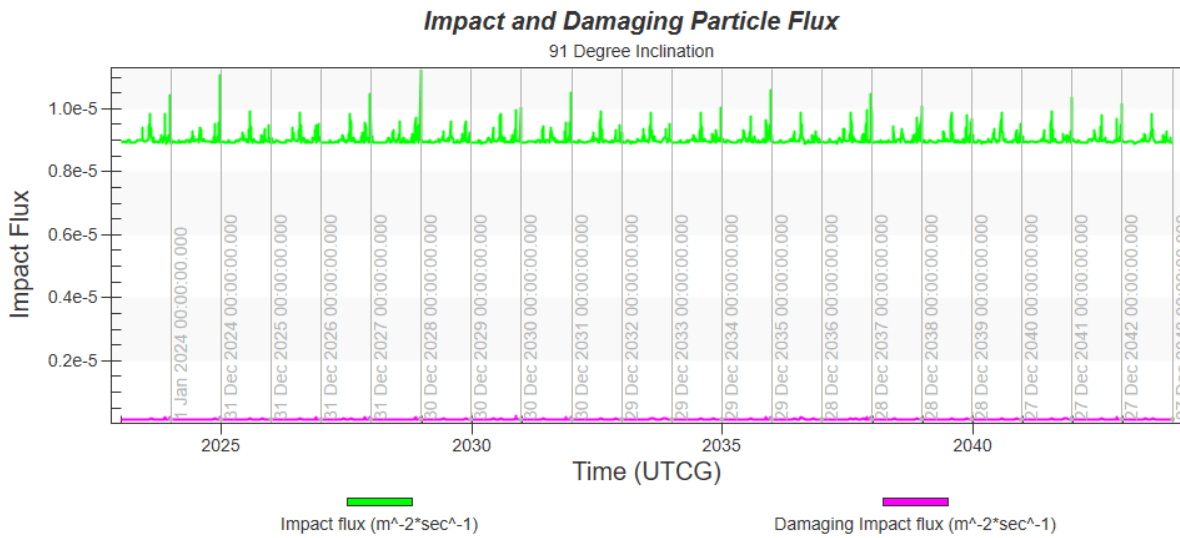


Figure 4.4: Impact Flux and Damaging Impact Flux vs Time at 91° Inclination

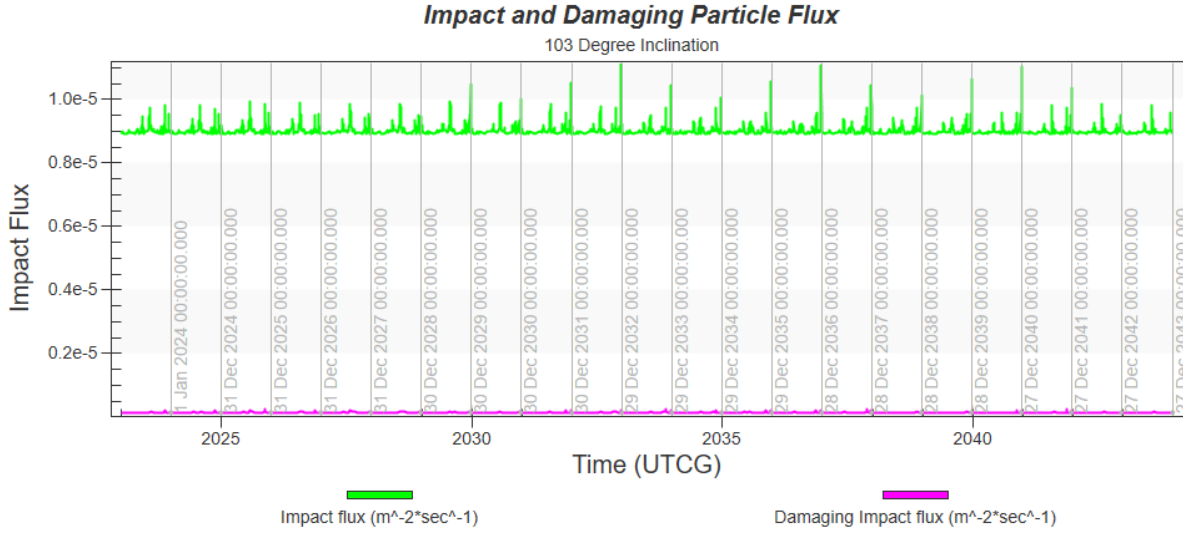


Figure 4.5: Impact Flux and Damaging Impact Flux vs Time at 103° Inclination

Table 4.2: Maximum Impact and Mass Flux for Micrometeorite Particles over Mission Duration

Damaging Impact Flux ($m^{-2} s^{-1}$)	Damaging Impact Mass Flux ($kg m^{-2} s^{-1}$)	Impact Flux ($m^{-2} s^{-1}$)	Impact Mass Flux ($kg m^{-2} s^{-1}$)
2.266×10^{-7}	1.634×10^{-16}	1.110×10^{-5}	2.356×10^{-16}

5. Thermal Analysis

While in orbit, POGSat will experience thermal loads due to radiative heat from the sun and Earth's albedo. As the spacecraft goes in and out of eclipse, temperatures will fluctuate. To verify the thermal conditions inside the spacecraft required for electronic operation were met, thermal analysis was conducted using STK and COMSOL Multiphysics. The temperature requirements of the spacecraft were determined by the operating ranges for electronic components. The operating temperature ranges of all electrical components are given in Table 5.1.

Table 5.1 Component Operating Temperatures

Component	Minimum Temperature	Maximum Temperature
Titan-1 Battery	-30° C	80° C
ISIS On Board Computer	-25° C	65° C
UHF Transceiver	-20° C	60° C
Iridium Transceiver	-40° C	85° C

Based on these requirements, it was determined the spacecraft temperature should remain in the range of -20° to 60° C.

The thermal analysis was conducted using two methods: the STK SEET tool, and a COMSOL Multiphysics simulation. The SEET tool provides a simple model of the spacecraft bulk temperature throughout an orbit, while COMSOL provides more detail of temperature distribution and transient effects.

5.1. SEET Thermal Analysis

STK SEET contains a vehicle temperature module which can compute the average equilibrium temperature of the spacecraft for a given position in the orbit. This tool works by treating the spacecraft as a single isothermal object and evaluates an energy balance between the heat radiated from the spacecraft and the incident radiation from the sun and Earth [50]. For the SEET simulation, the spacecraft was modeled as a sun-facing plate, as the sun facing side of the spacecraft would experience the greatest temperature change when passing in and out of eclipse. The emissivity and absorptivity properties of the material were set to those of aluminum with an absorptivity of 0.14 and emissivity of 0.03 [51]. The Earth albedo was set to an average value of 0.34. The SEET simulation produced the temperature plot shown in Figure 5.1.

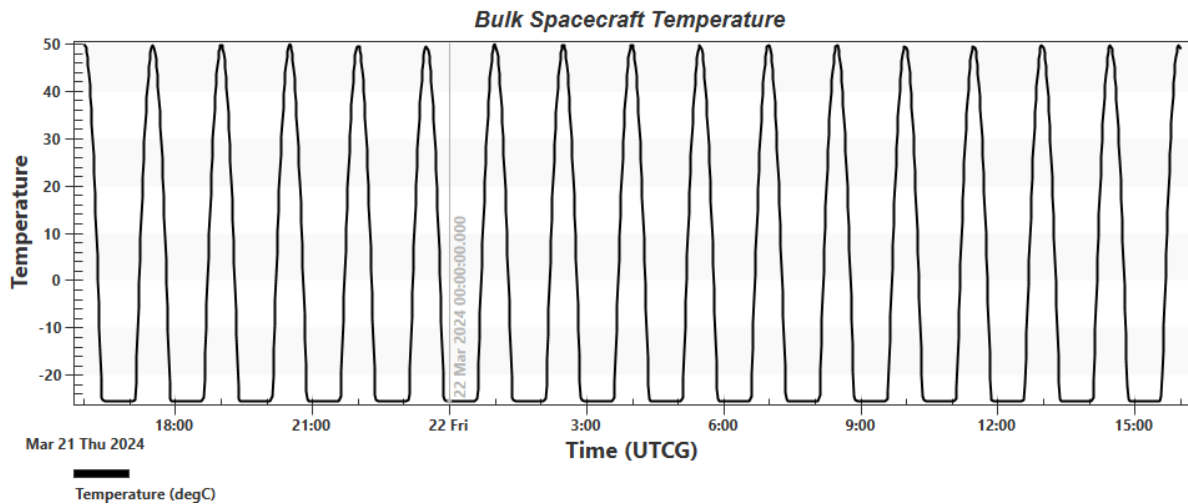


Figure 5.1 SEET Bulk Temperature with Aluminum Surface

SEET predicted the temperature to range from -25°C to 50°C over the course of an orbit. When the spacecraft is in eclipse, the temperature would drop below the operating limit of the computer and transceiver. Due to this, a thermal control mechanism would be required. The simplest way of passively controlling the spacecraft temperature would be to use a surface coating. A surface of Silver Beryllium

Copper with Teflon Overcoating has an absorptivity of 0.12, and emissivity of 0.38 [51]. Using these values in the SEET simulation gave the plot shown in Figure 5.2.

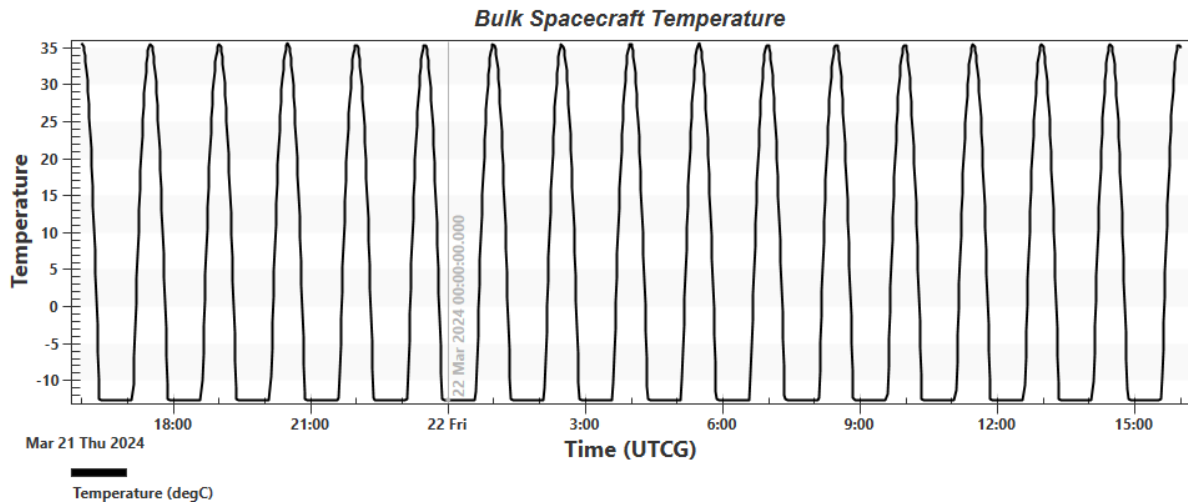


Figure 5.2 SEET Bulk Temperature with Silver Beryllium Coating

This surface coating gives a temperature range of -13°C to 35°C , well within the operating range of all electronics.

5.2. COMSOL Simulation

In addition to the SEET Thermal analysis, a COMSOL Multiphysics simulation was used to gather more detailed information which could be compared to the SEET results. The COMSOL simulation accounts for temperature variation throughout the spacecraft body, and models the transient behavior of heat transfer, rather than steady state results. The COMSOL simulation was set up using the Heat Transfer with Orbital Thermal Loads module, which is designed to simulate the thermal loads a spacecraft would experience in orbit. The project was modified from a spacecraft thermal analysis example project provided by COMSOL [52].

An extremely defeatured model of POGSat was created and imported into COMSOL as a form assembly geometry. Selections were defined for the space-facing boundaries, and internal boundaries. The spacecraft body was assigned to be aluminum and given the corresponding emissivity properties. The geometry was meshed using the “Extra Coarse” setting to reduce simulation runtime. The COMSOL geometry is shown in Figure 5.3.

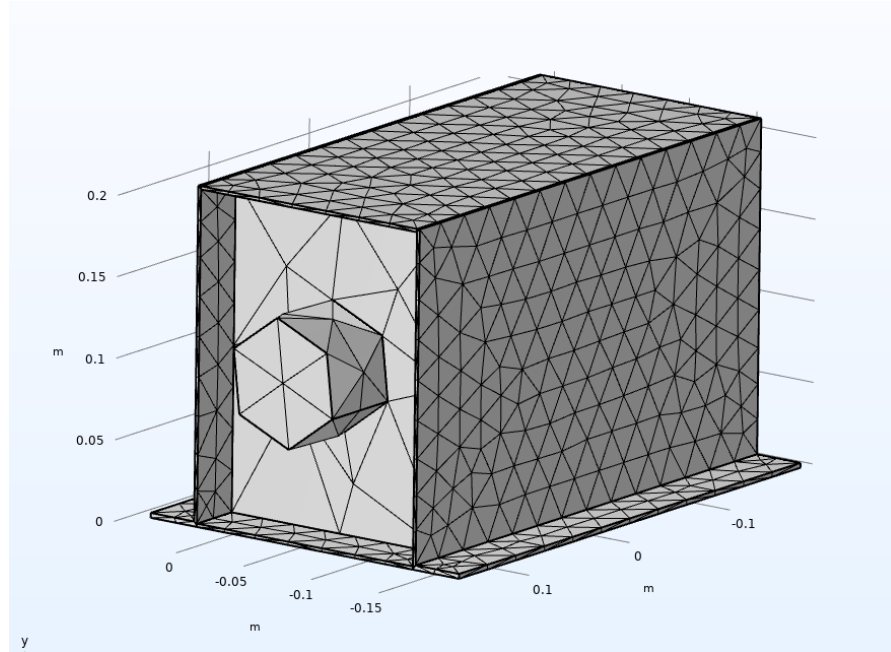


Figure 5.3 Meshed Geometry of COMSOL Simulation

The Orbital Thermal Loads module allows for the orbit and orientation of the spacecraft to be defined. The spacecraft was set to have a 260 km, 91° orbit, and the bottom face of the spacecraft was defined to be nadir facing. The simulation was run for a duration of four orbits, and temperature results were obtained. Figure 5.4 shows a plot of the maximum and minimum temperatures on the spacecraft over time.

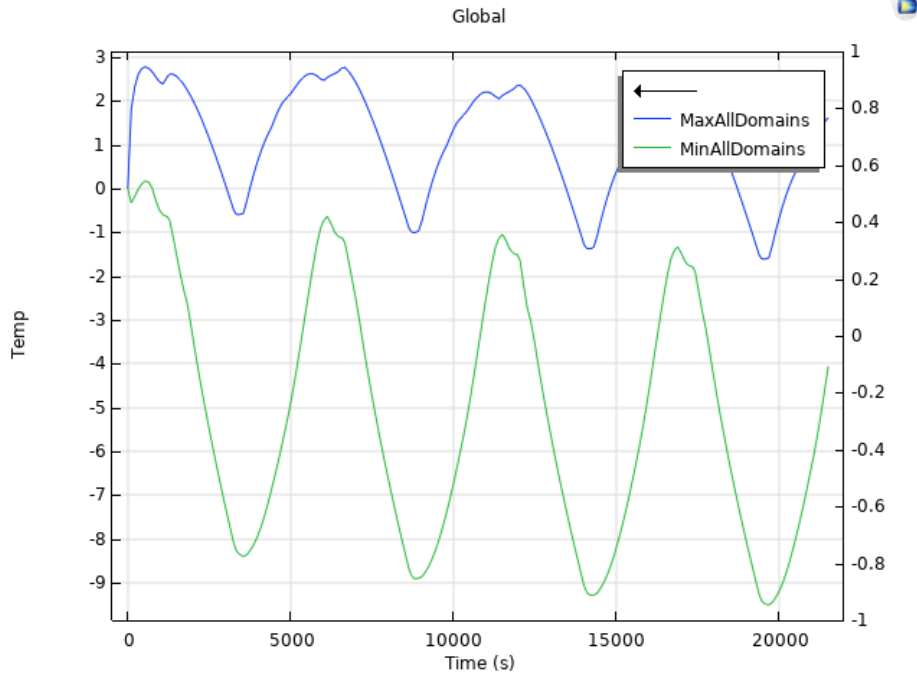


Figure 5.4 COMSOL Max and Min Temperatures

Between the maximum and minimum, the temperature ranges from -10°C to 3°C based on the COMSOL simulation. The COMSOL results predict much less temperature variation compared to the STK analysis. This is likely because the STK SEET tool only models the steady state temperature, which is what would occur if the spacecraft were to remain in the same position until thermal equilibrium is reached. The COMSOL simulation models the transient behavior of the temperature, so the spacecraft does not have time to heat to its maximum steady state temperature before entering eclipse.

6. Societal and Environmental Impacts

Climate change is a global challenge that affects all aspects of the physical world. Utilizing onboard sensors or imaging technology, satellites similar to the POGSat mission are able to provide current data on the state of the Earth's gravitational field. Accurate maps of the changes in the gravitational fields around Earth can be used to track the rate the landmasses are changing in mass, as the gravitational strength depends on the object's mass. Therefore, satellite observation and gravitational field measuring can help quantify climate change's effects on the Arctic ice caps.

One of the areas where satellite gravimetry can contribute to climate change research is the rate of ice-mass loss in the polar regions. The ice caps retain 69% of Earth's fresh water and reflect solar radiation, maintaining the Earth's temperature regulation and water storage [53]. However, due to temperature fluctuation from climate change, the glacier mass is decreasing at a substantial rate, with an approximate sea level increase of 0.8 mm per year from the Greenland Ice Sheet alone, with an accumulated sea level rise of 11.2 mm over a 14-year period. In order to measure the rate the ice mass is decreasing, gravimetric satellites such as GRACE and GRACE-FO can measure the gravitational field above a land mass, which directly corresponds to the amount of mass in the land below the satellite.

Currently, the GRACE mission series contributes primarily to the data utilized for gravitational field readings, while the more precise GOCE data is utilized primarily for oceanic geodesy [7]. As such, a mission developed with the increased accuracy of the GOCE mission optimized for gravitational mapping of the polar regions will increase the accuracy of the gravitational field results researchers use to chart ice mass depletion. The POGSat mission design can contribute gravitational field measurements on an 11-day basis, which provides approximately nine full data sets for each three month measurement period [53]. While current research indicates that a ten-year sampling period is sufficient in providing detail on the relevant effects of ice mass depletion, increasing the amount of data readings through an extended mission lifespan improves the overall reporting accuracy, allowing predictions about mass reduction and consequent sea level rise to be more informed [3,53].

7. Helmholtz Cage

In addition to the satellite's design, this project includes continuing development of a Helmholtz Cage, carrying on the work of previous MQPs. A Helmholtz cage is a device designed to generate a magnetic field that can be controlled to point along any direction [54]. The cage is composed of three pairs of coils of wire. Running current through the coils generates a magnetic field along the central axis of the coils. Using two coils parallel to each other generates a uniform magnetic field between the pair. Arranging three coil pairs along perpendicular faces allows for a magnetic field vector in any direction to be generated [54]. By using a computer simulation to control the magnetic field, the magnetic conditions experienced by a spacecraft can be generated, simulating an entire orbit. The cage enables hardware in the loop testing of an ADC system.

The Helmholtz cage at WPI began development in the 2021 CubeSat MQP [55]. The cage is comprised of six square coils of wire to form the electromagnets. Three DC power supplies are used to generate current for each coil pair. The power supplies are controlled using LabView software. The controlling software can run a simulation of what magnetic field would be expected and produce that field in the cage. A three-axis magnetometer placed within the cage would measure the field strength, and this signal would feed back to the software to form a control loop. To produce the desired field, the cage will also need to cancel the local earth magnetic field, which is why a feedback control system is necessary.

As of the start of this MQP, the cage was not fully functional due to issues with controlling the power supplies, and components not having the desired functionality. As part of this MQP, the team sought to improve the system with new components and measure a generated field. To aid in the testing process, a milligauss meter was purchased to measure the generated field and ensure its accuracy. Provided the magnetic field strength of the Earth at varying altitudes, a Gauss meter with a microgauss resolution is necessary to account for the low magnitude changes that occur at varying altitudes. The IDR-321 Geomagnetometer was selected as the most ideal Gauss meter for our application, as it was specifically designed for mapping magnetic field variation and supports a microgauss resolution [56]. Due

to the magnitude of the magnetic field strength, an accessory zero gauss chamber would also be required to ensure proper calibration, such as the one pictured alongside the IDR-321 in Figure 7.1. The Geomagnetometer was purchased to verify the magnetic field strength readings to ensure the measured data matches the reported data from the magnetometers.



Figure 7.1: IDR-321 Geomagnetometer with Hall Probe, pictured with accessory Zero Gauss Chamber

In addition to the geomagnetometer, a National Instruments Data Acquisition System (DAQ) was purchased to read measurements from a digital magnetometer to be displayed in LabView. Previously, a DAQ from LabJack was purchased, however it was found to be challenging to read data from the magnetometer over an I2C bus, and a more versatile DAQ was desired. As a replacement, the NI USB-6001 DAQ was chosen for its multiple analog and digital channels, and easy integration with LabView software [57].

8. Conclusions

The propulsion subsystem focused on the orbital maneuvers needed to perform the mission and determining the ideal inclinations to optimize mission performance and global coverage. The thruster-down select and a MATLAB program were created to show thruster viability. Preliminary calculations were determined for the Phase One transfer maneuvers. Upon selecting a final thruster, a full orbital model was built in STK to create an accurate maneuver and lifetime simulation, which established the required propellant mass as 5.33 kg of Iodine and 3.41 kg of Xenon and a final ΔV of 3.25 km/s. Additional STK lifetime simulations were performed to assess the practicality of the mission as it relates to the goal of measuring mass depletion of the polar ice caps, which extended Phase 2 data collection to 10 years.

The structures subsystem investigated the required CubeSat size and selected a satellite dispenser. The Canisterized Satellite Dispenser was selected for its loaded tab-based design which secures the satellite during launch, and flight heritage. A gradiometer payload was designed with six high precision accelerometers aligned at the center of mass. A CAD model of the satellite was created in SolidWorks to aid in the positioning and selection of components. Vibration simulations showed that the satellite would remain within the specifications of the dispenser.

The environmental analysis subsystem focused on ensuring that the internal components of the POGSat satellites would remain functional. Over a 20-year extended mission, 0.75 mm of aluminized mylar shielding prevented damaging levels of accumulated radiation and particulate flux. As such, with the inclusion of the shielding both POGSats are suited to perform within the atmospheric conditions of both inclinations.

9. References & Bibliography

1. *What Are SmallSats and CubeSats?* - NASA. www.nasa.gov/what-are-smallsats-and-cubesats/.
2. Purkhauser AF, Pail R. Triple-Pair Constellation Configurations for Temporal Gravity Field Retrieval. *Remote Sensing*. 2020; 12(5):831. <https://doi.org/10.3390/rs12050831>
3. Otosaka, I., et al. “Mass balance of the Greenland and Antarctic ice sheets from 1992 to 2020” *Earth System Science Data*, Vol 15, No. 4, 2023, pp. 1597-1616. <https://doi.org/10.5194/essd-15-1597-2023>
4. Johannessen, J. A., Balmino, G., Le Provost, C., Rummel, R., Sabadini, R., Sünkel, H., Tscherning, C. C., Visser, P., Woodworth, P., Hughes, C., Legrand, P., Sneeuw, N., Perosanz, F., Aguirre-Martinez, M., Rebhan, H., & Drinkwater, M. (2003). The European Gravity Field and Steady-State Ocean Circulation Explorer Satellite Mission Its Impact on Geophysics. *Surveys in Geophysics*, 24(4), 339–386. <https://doi.org/10.1023/B:GEOP.0000004264.04667.5e>
5. Spherical Harmonic Representation of the Gravity Field Potential 1 Introduction [Internet]. [cited 2023 Oct 3]. Available from: https://spsweb.fltops.jpl.nasa.gov/portaldataops/mpg/MPG_Docs/Source%20Docs/gravity-SphericalHarmonics.pdf
6. Flechtner, F., Reigber, C., Rummel, R. *et al.* Satellite Gravimetry: A Review of Its Realization. *Surv Geophys* **42**, 1029–1074 (2021). <https://doi.org/10.1007/s10712-021-09658-0>

7. GOCE - Earth Online [Internet]. earth.esa.int. Available from:
<https://earth.esa.int/eogateway/missions/goce>
8. Nie Y, Shen Y, Chen Q. Combination Analysis of Future Polar-Type Gravity Mission and GRACE Follow-On. *Remote Sensing*. 2019; 11(2):200.
<https://doi.org/10.3390/rs11020200>
9. Satellite Gravimetry [Internet]. GGOS. Available from: <https://ggos.org/item/satellite-gravimetry/>
10. GRACE - Earth Online [Internet]. earth.esa.int. Available from:
<https://grace.jpl.nasa.gov/mission/grace/>
11. GRACE Instruments - Earth Online [Internet]. earth.esa.int. Available from:
<https://earth.esa.int/eogateway/missions/grace#instruments-section>
12. Frommknecht, Björn & H, Oberndorfer & Flechtner, F. & R, Schmidt. (2003). Integrated sensor analysis for GRACE - Development and validation. *Advances in Geosciences*. 1. 10.5194/adgeo-1-57-2003.
13. B. D. Tapley, S. Bettadpur, M. M. Watkins and Ch. Reigber, The Gravity Recovery and Climate Experiment: Mission Overview and Early Results, *Geophys. Res. Lett.*, 31, L09607, doi:10.1029/2004GL019920, 2004.
14. GOCE Mission Requirements Document Noordwijk The Netherlands [Internet]. 2000 [cited 2023 Oct 3]. Available from: <https://esamultimedia.esa.int/docs/GO-RS-ESA-SY-0001.PDF>
15. Massotti, L., Bulit, A., Daras, I., Carnicero Dominguez, B., Carraz, O., Hall, K., Heliere, A., March, G., Marchese, V., Martimort, P., Palmer, K., Rodrigues, G., Silvestrin, P., and Wallace, N.: Next Generation Gravity Mission design activities within the MAGIC -

MAsS Change and Geoscience International - Constellation, EGU General Assembly 2023, Vienna, Austria, 24–28 Apr 2023, EGU23-14482, <https://doi.org/10.5194/egusphere-egu23-14482>, 2023.

16. Craig, C. CubeSats for Environmental Monitoring (Conference Presentation), Proc. SPIE 11530, Sensors, Systems, and Next-Generation Satellites XXIV, 1153002 (23 September 2020); <https://doi.org/10.1117/12.2582821>
17. Siemens, C. GOCE Gradiometer Calibration and Level 1b Data Processing. ESA. Noov 2011. <https://earth.esa.int/eogateway/documents/20142/37627/GOCE-gradiometer-calibration-and-level-1b-data-processing.pdf>
18. The Sun sets on the Arctic melt season - National Snow and Ice Data Center [Internet]. nsidc.org. Available from: <https://nsidc.org/arcticseaicenews/2023/10/the-sun-sets-on-the-arctic-melt-season/>
19. Missions Launched [Internet]. Rocket Lab. 19 Feb 2024 Available: <https://www.rocketlabusa.com/missions/missions-launched/>
20. The Kick Stage: Responsible Orbital Deployment [Internet]. Rocket Lab. [cited 2023 Dec 16]. Available from: <https://www.rocketlabusa.com/updates/the-kick-stage-responsible-orbital-deployment/>
21. Launch: Payload User’s Guide [Internet]. RocketLab. 2020. Available from: <https://www.rocketlabusa.com/assets/Uploads/Rocket-Lab-Launch-Payload-Users-Guide-6.5.pdf>
22. Federal Communications Commission. (2022, September 29). FCC Adopts New '5-Year Rule' For Deorbiting Satellites To Address Growing Risk Of Orbital Debris. FCC Adopts

New '5-Year Rule' for Deorbiting Satellites. Retrieved from

<https://www.fcc.gov/document/fcc-adopts-new-5-year-rule-deorbiting-satellites>

23. Space debris: Feel the burn. ESA. (2021, April 28). Retrieved October 5, 2023, from
om

https://www.esa.int/Space_Safety/Clean_Space/Space_debris_feel_the_burn#.Y_j2QJRRAL8.link

24. G. Sobreviela-Falces et al., "A Navigation-Grade Mems Vibrating Beam Accelerometer,"
2022 IEEE 35th International Conference on Micro Electro Mechanical Systems
Conference (MEMS), Tokyo, Japan, 2022, pp. 782-785, doi:
10.1109/MEMS51670.2022.9699447.

25. RocketLab. *Canisterized Satellite Dispenser (CSD) Data Sheet*. 23 May 2022.

26. Canisterized Satellite Dispenser Payload Specification [Internet]. RocketLab. Available
from: <https://www.rocketlabusa.com/assets/Uploads/PSC/Rocket%20Lab%20PSC%20-%202002367F%20Payload%20Spec%20for%203U%206U%2012U.pdf>

27. 12U SUPERNOVA Structure Kit [Internet]. Orbital Transports. [cited 2023 Dec 16].
Available from: <https://catalog.orbitaltransports.com/12u-supernova-structure-kit/>

28. Solar Arrays [Internet]. MMA Design LLC. Available from:
<https://mmadesignllc.com/products/solar-arrays/>

29. Ansys Government Initiatives, "Adding articulations for STK and Cesium" (Oct, 2020)
[Online Video] Available
https://www.youtube.com/watch?v=Lzpr3qQQ4eo&ab_channel=AnsysGovernmentInitiatives%28AGI%29

30. Piper, L. Prigge, E. “Design of a Polar Orbiting Gravimetry Cubesat” Worcester Polytechnic Institute, Worcester 2024.
31. Sutton, G. P., & Biblarz, O. (2017). *Rocket Propulsion Elements*. John Wiley & Sons, Inc.
32. *BGT-X5 monoprop*. Busek Co. Inc. (n.d.). Retrieved October 10, 2023, from https://static1.squarespace.com/static/60df2bfb6db9752ed1d79d44/t/61292af2a097083a87c4cbc0/1630087925107/BGT_X5_v1.0.pdf
33. Krejci, D., Mier-Hicks, F., Fucetola, C., Lozano, P., Hsu Schouten, A., and Martel, F. “Design and Characterization of a Scalable ion Electrospray Propulsion System,” ISTS Paper b-149, July 2010. https://electricrocket.org/IEPC/IEPC-2015-149_ISTS-2015-b-149.pdf
34. *nanoFEEP*. Morpheus Space (n.d.). Retrieved October 10, 2023, from <https://satcatalog.s3.amazonaws.com/components/981/SatCatalog - Morpheus Space - nanoFEEP - Datasheet.pdf?lastmod=20210710023905>
35. *BHT-100 Hall Effect Thruster*. Busek Co. Inc. (n.d.). Retrieved December 15, 2023, from https://static1.squarespace.com/static/60df2bfb6db9752ed1d79d44/t/6154811d7ac4036af765f736/1632928031263/BHT_100_v1.0.pdf
36. Becatti, G., Pedrini, D., Kasoji, B., Paganucci, F., Andrenucci, M. “Triple Langmuir Probes Measurements of LaB6 Hollow Cathodes Plume,” *Frontiers in Physics*, Vol 7, 2019. Retrieved from <https://doi.org/10.3389/fphy.2019.00027>

37. *NPT30-12-1U Smart Iodine Electric Propulsion System*. ThrustMe (2021). Retrieved

December 15, 2023, from

https://www.thrustme.fr/base/stock/ProductBannerFiles/2_thrustme-npt30-i2.pdf

38. K. A. Polzin and S. Peeples, “Iodine Hall Thruster Propellant Feed System for a

CubeSat,” AIAA/ASME/SAE/ASEE Joint Propulsion Conference, Jul. 28, 2014.

Retrieved from <https://ntrs.nasa.gov/citations/20140012577>.

39. Tempco. “Kapton Catalog Pages – Flexible Heaters” [PDF file], (2023), Retrieved

February 19, 2024 from [https://www.tempco.com/Tempco/Resources/09-Flexible-](https://www.tempco.com/Tempco/Resources/09-Flexible-Resources/KaptonCatalogPages.pdf)

[Resources/KaptonCatalogPages.pdf](https://www.tempco.com/Tempco/Resources/09-Flexible-Resources/KaptonCatalogPages.pdf).

40. Special Metals. “INCONEL® Alloy X-750” [PDF file], (2004) Retrieved March 2, 2024

from <https://www.specialmetals.com/documents/technical-bulletins/inconel/inconel->

[alloy-x-750.pdf](https://www.specialmetals.com/documents/technical-bulletins/inconel/inconel-alloy-x-750.pdf)

41. Saravia, M.M.; Bernazzani, L.; Ceccarini, A.; Vinci, A.E.; Paganucci, F. Modeling and

Characterization of a Thermally Controlled Iodine Feeding System for Electric

Propulsion Applications. *Aerospace* 2020, 7, 10.

<https://doi.org/10.3390/aerospace7020010>

42. VACCO Industries. "High Pressure Latch Valves" [PDF File] (2004) Retrieved March 2, 2024 from: https://www.vacco.com/images/uploads/pdfs/latch_valves_high_pressure.pdf
43. VACCO Industries. "Low Pressure Latch Valves" [PDF File] (2004) Retrieved March 2, 2024 from: https://www.vacco.com/images/uploads/pdfs/latch_valves_low_pressure.pdf
44. TE Connectivity. "PTF Temp Sensors Datasheet" [PDF File] (2017) Retrieved March 2, 2024 from: https://www.tti.com/content/dam/ttiinc/manufacturers/te-sensor-solutions/PDF/ptf_temp_sensors_datasheet.pdf
45. Rafalskyi, D., Martínez, J.M., Habl, L. et al. In-orbit demonstration of an iodine electric propulsion system. *Nature* 599, 411–415 (2021). Retrieved from <https://doi.org/10.1038/s41586-021-04015-y>
46. *Gravity Field and Steady-State Ocean Circulation Mission*. ESA (1999). ESA SP-1233 (1), July 1999. Retrieved from https://esamultimedia.esa.int/docs/goce_sp1233_1.pdf
47. Bickett, William J., "Aerodynamic effects of integrated lifting surfaces on very low Earth orbit small satellites" (2019). Theses. 298. Retrieved from <https://louis.uah.edu/uah-theses/298>

48. Buis, A. (2019, Oct 2). *Earth's Atmosphere: A Multi-layered Cake*. NASA. Retrieved from <https://climate.nasa.gov/news/2919/earths-atmosphere-a-multi-layered-cake/#:~:text=in%20the%20thermosphere,-.Exosphere.,merges%20with%20the%20solar%20wind>
49. Duderstadt, K., Huang, C., Spence, H., Smith, S., Blake, J., Crew, A., Johnson, A., Klumpar, D., Marsh, D., Sample, J., Shumko, M., Vitt, F., (2021, March 11). Estimating the Impacts of Radiation Belt Electrons on Atmospheric Chemistry Using FIREBIRD II and Van Allen Probes Observations. *JGR Atmospheres*, Vol 126, No. 7, 2021. Retrieved from <https://doi.org/10.1029/2020JD033098>
50. Analytical Graphics, Inc. (AGI), "STK Space Environments Effects Tool (SEET)," 2020. [Online]. Retrieved from https://help.agi.com/stk/11.0.1/stktraining/pdf/SEET_manual.pdf
51. L. Kauder. "Spacecraft Thermal Control Coatings References", NASA/TP-2005-212792, Dec 2005. [accessed Feb. 20, 2024]
52. COMSOL "Spacecraft Thermal Analysis" [Online] Available <https://www.comsol.com/model/spacecraft-thermal-analysis-109811>
53. Taking a Measure of Sea Level Rise: Gravimetry. NASA Earth Observatory. (2021, April 28). Retrieved from <https://earthobservatory.nasa.gov/images/147437/taking-a-measure-of-sea-level-rise->

[gravimetry#:~:text=The%20method%20that%20most%20directly,on%20a%20pair%20of%20satellites](#)

54. DA SILVA, Rodrigo Cardoso, ISHIOKA, Igor Seiiti Kinoshita, CAPPELLETTI, Chantal, BATTISTINI, Simone and BORGES, Renato Alves (2019). Helmholtz cage design and validation for nanosatellites HWIL testing. *IEEE Transactions on Aerospace and Electronic Systems*, 55 (6), p. 1.
55. Mileti, Robatzek, A. L., Brown, A. R., St Jean, M., Cooley, W. R., Messey, S. E., & Klenk, A. D. (2021). *Magnetospheric Nanosat Design*. Worcester Polytechnic Institute.
56. Geomagnetometer: IDR-321(w/Hall Probe). Integrity Design, (n.d.) Retrieved December 16, 2023, from <http://www.integritydesign.com/images/Integrity/datasheet%20Geomagnetometer.pdf>
57. LabView USB-6001, National Instruments. Available <https://www.ni.com/en-us/shop/model/usb-6001.html>

10. Appendices

Appendix A

Thruster Master List

Thruster	Type	Propellant Type	Manufacturer	Heritag	Max Power	Isp (sec)	It (Nsec)	Thrust	Wet Mass	Dry Mass (kg)	Volume (U)	Datash
A4 CubeDrive	Biprop		Dawn Aerospace	Yes	12.5	285	425		1.17	0.97	0.8	[1]
MPS-120-1U	Monoprop	Hydrazine	Aerospace Rocketd	No	30	206	810	4	1.6	1.2	1	[2]
MPS-120-2U	Monoprop	Hydrazine	Aerospace Rocketd	No	30	200	1960	4	2.5	1.5	2	[2]
MPS-130-2U	Alternativ	Ascent	Aerospace Rocketd	No	39	198	2720	4	2.8	1.4	2	[3]
MPS-130-1U	Alternativ	Ascent	Aerospace Rocketd	No	39	192	1130	4	1.7	1.1	1	[3]
HYDROS-C	Alternativ	Water	Tethers Unlimited	Yes	25	310	2151	1.2	2.7	2.2	2.6	[4]
EPSS C2	Alternativ	ADN Blend	NanoAvionics	No	8	214	1700	1	2.5	1.7	2	[5]
Starling cold 2U	Cold Gas		Benchmark Space	No	15	70	240	1	2.7	2.35	2	[6]
Starling cold 1U	Cold Gas		Benchmark Space	No	15	70	100	1	1.5	1.35	1	[6]
Starling cold 0.5	Cold Gas		Benchmark Space	No	15	70	40	1	0.75	0.69	0.5	[6]
CubeSat 2U Mk3	Alternativ	N2O and C3H6	Dawn Aerospace	Yes	12	285	2200	0.5	2.4	1.6	2	[7]
CubeSat 1.5U Mk3	Alternativ	N2O and C3H6	Dawn Aerospace	Yes	12	285	1500	0.5	1.85	1.3	1.5	[7]
CubeSat 1U Mk3	Alternativ	N2O and C3H6	Dawn Aerospace	Yes	12	285	850	0.5	1.41	1.1	1	[7]
CubeSat 0.8U Mk3	Alternativ	N2O and C3H6	Dawn Aerospace	Yes	12	285	425	0.5	1.17	1	0.8	[8]
BGT-X5	Alternativ	Ascent	Busek	No	20	225	565	0.5	1.5	1.24	1	[9]
Monopropellar	Alternativ	Green	Moog	No	45	224	500	0.5	1.01	0.78	1	[10]
Monopropellar	Monoprop	Hydrazine	Moog	No	45	224	500	0.5	1.01	0.78	1	[10]
Aerojet GR-1	Alternativ	Ascent	Aerospace Rocketd	Yes	12	235	23,000	0.4				
C-POD	Cold Gas	R134a	VACCO	Planned	5	40	186	0.2	1.24	0.77	1	[12]
MPUC 2U	Alternativ	CMP-10	CU Aerospace	No	3	180	2460	0.16	3.22	1.85	2	[13]
MPUC 1.5U	Alternativ	CMP-10	CU Aerospace	No	3	180	1550	0.16	2.46	1.6	1.5	[13]
Standard MiPS	Cold Gas	R236fa	VACCO	No	12	40	515	0.1	2.46	1.14	1.4	[14]
Standard MiPS	Cold Gas	R236fa	VACCO	No	12	40	336	0.1	1.81	0.96	1	[15]
Standard MiPS	Cold Gas	R236fa	VACCO	No	12	40	219	0.1	1.36	0.8	0.7	[15]
Standard MiPS	Cold Gas	R236fa	VACCO	No	12	40	82	0.1	0.85	0.64	0.4	[15]
CuSP	Cold Gas	R134a	VACCO	Planned	12	40	69.4	0.1	0.69	0.51	0.3	[16]
NanoProp 6DC	Cold Gas	Butane	GOMSpace	Planned	15	50	100	0.06	0.8	0.68	1	[17]
MEPSI MiPS	Cold Gas	R236fa	VACCO	Yes	12	40	23	0.053	0.51	0.46	0.3	[18]
NanoProp200C	Cold Gas	Butane	GOMSpace	Yes	15	50	40	0.04	0.45	0.38	0.5	[19]
MarCO MiPS	Cold Gas	R236fa	VACCO	Yes	15	40	755	0.025	3.49	1.57	2	[20]
Comet 1000	Alternativ	Water	Bradford Space	No	25	185	1155	0.017	1.44	0.74	2.6	[21]
BHT-100	Hall Effect		Busek	No	100	1000	45000	0.007	1.16	1.16		[22]
ExoMG nano L	Hall Effect	Xenon	Exotrail	No	60	800	5400	0.0025	3.5	2.81	2	[23]
ExoMG nano S	Hall Effect	Xenon	Exotrail	No	60	800	900	0.0025	2	1.89	1	[23]
NPT30-I2-1.5U	Ion	Iodine	ThrustMe	Yes (var)	65	2400	9500	0.0011	1.7	1.3	1.5	[24]
NPT30-I2-1U	Ion	Iodine	ThrustMe	Yes	65	2400	5500	0.0011	1.2		1	[24]
BIT-3	Ion	Iodine	Busek	Planned	75	2150	31637	0.0011	2.9	1.4	1.6	[25]
MultiFEEP for C	Electrospr	Gallium (FEEP)	Morpheus	No	87	7000	46000	0.001	2.2	1.53	2	[26]
BET-MAX	Electrospray		Busek	Yes	24	850	92	0.0006	0.8	0.79	1.7	[27]
TILE-2	Electrospr	EMI-BF4	Accion Systems	Yes	20	755	1650	0.00045	1.25	1.2	1	[28]
MultiFEEP for E	Electrospr	Gallium (FEEP)	Morpheus	No	22	7000	11500	0.00025	0.5	0.33	0.5	[26]
NanoFEEP (inte	Electrospr	Gallium (FEEP)	Morpheus	Yes	12	7000	13600	0.00016	0.8	0.64	1	[26]
NanoFEEP (inte	Electrospr	Gallium (FEEP)	Morpheus	Yes	12	7000	13600	0.00016	0.8	0.64	1	[26]
SIEPS	Electrospr	Ionic (inc. Ascent)	MIT	Yes	1.5	1150		0.000074			0.15	[29]
BET-1mN	Electrospray		Busek	No	15	800		0.00007			0.38	[30]
NanoFEEP	Electrospray		Morpheus	Yes	3	7000	3400	0.00004	0.2	0.16	0.25	[26]
TILE-2	Electrospr	EMI-BF4	Accion Systems	Yes	4	1650	21	0.00004	0.48	0.48	0.5	[31]

Appendix B

Impulsive Phase One Transfer Maneuver MATLAB Code

```
%Constants
g = 9.81; %m/s^2
pi = 3.14;

%Inputs

Isp = 225; %sec
T = 0.5; %N

mi = 24; %kg, for a 12U
rho_p = 1490; %density, kg/m^3

alt_i = 500*10^3; %initial altitude (m)
alt_f = 260*10^3; %final altitude (m)
r_E = 6.37814*10^6; %(m)
mu_E = 3.986*10^14; % standard gravitational parameter (m^3/s^2);

%Maneuver Calculations

r_t_1 = r_E + alt_i;
r_t_2 = r_E + alt_f;
a_t = (r_t_1+r_t_2)/2;

v_i_1 = sqrt(mu_E/r_t_1);
v_f_2 = sqrt(mu_E/r_t_2);
v_t_1 = sqrt(mu_E*((2/r_t_1)-(1/a_t)));
v_t_2 = sqrt(mu_E*((2/r_t_2)-(1/a_t)));
DelV_1 = v_t_1-v_i_1;
DelV_2 = v_f_2 - v_t_2;
TotalDelV = abs(DelV_1) + abs(DelV_2);

%Altitude Change Propellant Use

c = Isp*g; %m/s
mf_alt = mi*exp(-(abs(TotalDelV))/c); %kg
mp_alt = (1-mf_alt/mi)*mi; %kg
MR_alt = exp((abs(TotalDelV))/c); %unitless ratio
mp_mi_alt = 1- mf_alt/mi; %unitless ratio
tb_alt = ((mp_alt*g*Isp)/T)/86400;
m_dot_alt = T/(g*Isp);
V_fuel_alt = (mp_alt/rho_p);
```

Appendix C

Finite Phase One Transfer Maneuver MATLAB Code

```
% Constants
g = 9.81; %m/s^2
pi = 3.14;

% Inputs

Isp = 2400; %sec
T = 0.0011 %N
cathode_m_dot = 1*(10^-7); %kg/s

mi = 24; %kg, for a 12U
rho_p = 4930; %density, kg/m^3
rho_cathode = 1660; %density xenon, kg/m^3

alt_i = 500*10^3; %initial altitude (m)
alt_f = 260*10^3; %final altitude (m)
r_E = 6.37814*10^6; %m
mu_E = 3.986*10^14; % standard gravitational parameter (m^3/s^2);
theta = deg2rad(0); %inclination change, rad

% Maneuver Calculations

r_t_1 = r_E + alt_i;
r_t_2 = r_E + alt_f;
a_t = (r_t_1+r_t_2)/2;

v_i_1 = sqrt(mu_E/r_t_1);
v_f_2 = sqrt(mu_E/r_t_2);
v_t_1 = sqrt(mu_E*((2/r_t_1)-(1/a_t)));
v_t_2 = sqrt(mu_E*((2/r_t_2)-(1/a_t)));

DelV_1 = sqrt(v_t_2^2+v_f_2^2-2*v_t_2*v_f_2*cos(theta));
TotalDelV = abs(DelV_1);

% Altitude Change Propellant Use

c = Isp*g; %m/s
mf_alt = mi*exp(-(abs(DelV_1))/c); %kg
mp_alt = (1-mf_alt/mi)*mi; %kg
MR_alt = exp((abs(DelV_1))/c); %unitless ratio
mp_mi_alt = 1- mf_alt/mi; %unitless ratio
tb_alt = ((mp_alt*g*Isp)/T)/86400;
m_dot_alt = T/(g*Isp);
V_fuel_alt = (mp_alt/rho_p);

% Cathode Propellant Use

m_cathode_alt = cathode_m_dot*(tb_alt*86400);
V_cathode_alt = ((m_cathode_alt/rho_cathode))*1000000; %cm^3
cathode_tank_alt = V_cathode_alt/1000; %U
```